AD-A045 536   GENERAL ELECTRIC CO   PHILADELPHIA PA RE-ENTRY AND ENV--ETC F/G 11/3
CHEMICAL VAPOR DEPOSITION OF SILICON NITRIDE.(U)
SEP 77   R A TANZILLI, J J GEBHARDT, J O HANSON   N00014-76-C-0547
77SDR2257

UNCLASSIFIED

NL

1 OF 1
AD
A045536

Document No. 77SDR2257

CHEMICAL VAPOR DEPOSITION

OF

SILICON NITRIDE

September 1977

Summary Report

1 April 1976 - 31 August 1977

Prepared under Contract No. N00014-76-C-0547

for the

OFFICE OF NAVAL RESEARCH
800 N. Quincy Street
Arlington, Va. 22217

GENERAL ELECTRIC
Re-entry & Environmental
Systems Division
P. O. Box 7680
Philadelphia, Pa. 19101

D D C
RECEIVED
OCT 26 1977
B

AD A045536

Document No. 77SDR2257

CHEMICAL VAPOR DEPOSITION

OF

SILICON NITRIDE

September 1977

Summary Report

1 April 1976 - 31 August 1977

Prepared under Contract No. N00014-76-C-0547

for the

OFFICE OF NAVAL RESEARCH
800 N. Quincy Street
Arlington, Va. 22217

DDC
RECEIVED
OCT 26 1977
B

REPORT DOCUMENTATION PAGE		READ INSTRUCTIONS BEFORE COMPLETING FORM
1. REPORT NUMBER	2. GOVT ACCESSION NO.	3. RECIPIENT'S CATALOG NUMBER
4. TITLE (and Subtitle) CHEMICAL VAPOR DEPOSITION OF SILICON NITRIDE.		5. TYPE OF REPORT & PERIOD COVERED Technical 1 Apr 1976 thru 31 Aug 1977
		6. PERFORMING ORG. REPORT NUMBER Doc. No. 77SDR2257
7. AUTHOR(s) R. A. Tanzilli, J. J. Gebhardt, J. O. Hanson		8. CONTRACT OR GRANT NUMBER(s) N00014-76-C-0547
9. PERFORMING ORGANIZATION NAME AND ADDRESS General Electric Co., RESD P.O. Box 7560 Philadelphia, Pa. 19101		10. PROGRAM ELEMENT, PROJECT, TASK AREA & WORK UNIT NUMBERS NR-008-001/12 2-75(471)
11. CONTROLLING OFFICE NAME AND ADDRESS Office of Naval Research 800 N. Quincy Street Arlington, Va. 22217		12. REPORT DATE September 1977
		13. NUMBER OF PAGES 72
14. MONITORING AGENCY NAME & ADDRESS(if different from Controlling Office)		15. SECURITY CLASS. (of this report) Unclassified
		15a. DECLASSIFICATION/DOWNGRADING SCHEDULE

16. DISTRIBUTION STATEMENT (of this Report)

Approved for Public Release; distribution unlimited

17. DISTRIBUTION STATEMENT (of the abstract entered in Block 20, if different from Report)

18. SUPPLEMENTARY NOTES

19. KEY WORDS (Continue on reverse side if necessary and identify by block number)

Silicon nitride, chemical vapor deposition, electromagnetic properties, flexure strengths, microhardness

20. ABSTRACT (Continue on reverse side if necessary and identify by block number)

Experimental work during the past year has established the basic processing outlines for the deposition of crystalline alpha-Si_3N_4 plates and dome geometries. Preliminary correlations between critical processing variables and microstructure have been established. Property evaluations of deposits include: flexure strength, Young's moduli, thermal expansion, electromagnetic transmittance and reflectance, microhardness and fracture toughness deduced from indentation and grooved double-cantilever beam experiments.

DD FORM 1473 1 JAN 73 EDITION OF 1 NOV 65 IS OBSOLETE

404 884

Table of Contents

List of Illustrations

List of Illustrations

List of Illustrations

List of Tables

FOREWORD

SECTION I

INTRODUCTION

During the past year under Contract No. N00014-76-C-0547, the basic processing outlines for the fabrication of α-Si$_3$N$_4$ plate and dome geometries by the chemical vapor deposition (CVD) method have been determined. Physical property evaluations of deposits on this program when combined with earlier property data (as shown in Table 1) suggest that continued development and evaluation of CVD α-Si$_3$N$_4$ should be pursued since an optimized form could possess several unique attributes to be potentially useful as a high performance ceramic component in advanced DoD missile systems.

As documented in subsequent paragraphs, the first year's program broadly explored processing conditions which yielded crystalline CVD α-Si$_3$N$_4$ deposits suitable for material characterization. Preliminary correlations between major processing variables and microstructure have now been established. Both flat plate and dome configurations were successfully synthesized on the program. From selected deposits, physical property specimens were extracted and subsequently ground and polished. Property evaluations at room temperature documented in this report include: flexure strength, failure strain, Young's moduli, microhardness, visible and infrared transmittance, infrared reflectance, dielectric constant and loss tangent, and fracture toughness deduced from identation and grooved double-cantilever experiments.

Table 1. Physical Property Trends for CVD α-Si$_3$N$_4$

	Category	Supporting Data	Source
1.	Visible/Infrared Transmittance	Ground and polished translucent flat plate and dome geometries exhibit a transmittance window from 0.20 to 5.0 μm. (Conventional Si$_3$N$_4$ is opaque in this wavelength range.)	This work
2.	Radar Transmittance	High-purity deposits show a loss tangent at X-band approximately an order of magnitude lower than conventional Si$_3$N$_4$.	This work
3.	Oxidation Resistance	Oxidation studies monitored by weight gain measurements show a rate of 10^{-4} kg/m^{2}s$^{1/2}$ at 1450°C, or about 10 times less than Si$_3$N$_4$ hot-pressed with 5% MgO and tested at 1100°C.	Reference 1
4.	Creep Behavior	Creep experiments in three point bending at 1540°C showed essentially no deflection after 7 x 10^5 sec. at 70 MPa. The material exhibited an upper creep rate at least 5 orders of magnitude less than that expected for hot-pressed Si$_3$N$_4$ containing MgO, based on extrapolation of published data.	Reference 1
5.	Flexure Strength	Although room temperature flexure strength of CVD α-Si$_3$N$_4$ (at its current development stage in our laboratory) is approximately 1/3 that of hot-pressed Si$_3$N$_4$, its invariancy after a 100 hr. exposure at 1400°C is far superior to hot-pressed Si$_3$N$_4$ which generally exhibits a 50% reduction in flexure strength under similar aging conditions.	This work
6.	Microhardness	Crystalline CVD α-Si$_3$N$_4$ has a hardness level superior to common abrasives ranking it in third place behind diamond and cubic boron nitride; amorphous CVD α-Si$_3$N$_4$ has a hardness level comparable to α-Al$_2$O$_3$.	This work, Ref. 2
7.	Thermal Stress Resistance	Using standard thermal-stress resistant figure-of-merit parameters, Si$_3$N$_4$ is predicted to have good thermal stress resistance. Of course, its actual performance will depend upon specific test conditions and configurations.	Reference 3

2.

Table 1. Physical Property Trends for CVD α-Si$_3$N$_4$ (continued)

Category	Supporting Data	Source
8. Fracture Toughness	The critical stress intensity factor (Kc) of current generation CVD α-Si$_3$N$_4$ prepared on this program has been found to be comparable to hot-pressed Si$_3$N$_4$ using the NRL grooved double-cantilever beam method (K$_c$ = 4.3 MPa $\sqrt{m}$), but somewhat lower than hot-pressed Si$_3$N$_4$ using the RI identation toughness method (K$_c$ = 3.2 MPa $\sqrt{m}$).*	This work

*Resolution of the apparent discrepancies between the two test methods is currently under study.

3.

SECTION II

DEPOSITION CHEMISTRY

2.1 General Considerations

The deposition of non-crystalline silicon nitride from the vapor phase for use as passivating layers in integrated circuitry has been developed into a routine industrial step in the semiconductor industry. However, establishment of process requirements for producing crystalline deposits of significant thickness and controlled geometry and properties has not progressed to this point. Some experimental work has been done which has yielded sufficient material for characterization of optical, hardness and electrical properties, while basic studies are only recently being reported regarding deposition mechanism, deposition conditions and the relationships between properties and production.

Silicon nitride for semiconductor applications is usually produced by the interaction of silane (SiH_4) and ammonia (NH_3) at high dilutions in hydrogen in a rapidly moving gas stream at one atmosphere.[4, 5] Growth rates are of the order of 100 $\overset{o}{A}$ to 500 $\overset{o}{A}$ per minute, and deposit thicknesses of several micrometers are usually sought.

Deposition temperatures between 700 and $1000^{o}C$ are customary in so-called cold wall reactors while heating is confined to the substrate to be coated rather than including the entire enclosure.

However, for deposition of crystalline material of millimeter thicknesses, higher temperatures are required, where the low thermal stability of silane and the difficulty of handling it in high concentrations, militates against its convenient use. Furthermore, the coating of large shapes such as radomes or deposition of monolithic contours would be expected to be difficult to control in the cold-wall, atmospheric pressure reactors used in depositing thin films; thus, relatively large isothermally heated furnace enclosures appear to be more practical for such processing. This necessitates investigation of the formation of silicon nitride under so-called "hot-wall" conditions where the chemistry of formation is somewhat more complex because of the longer residence times,

4.

higher concentrations, complex flow patterns, slower transport rates and by-product formation.

This report deals with studies of the formation of crystalline α-silicon nitride in a hot wall reactor system, using a variety of silicon precursor materials, conducted for the purpose of establishing a process base on which to develop optimized deposition conditions for production of useful shapes and coatings of silicon nitride for various electromagnetic applications.

2.2   Chemistry of Silicon Nitride Formation

Powdered, commercial grade silicon nitride used for hot-pressing of ceramic ware (tubes, crucibles, etc.) is made by reaction of silica and ammonia in the presence of carbon. A relatively crude, impure product results which is not amenable to subsequent formation of the materials of interest to this program. Consequently, chemical vapor deposition, with its dependence on pure, vapor-borne precursor materials, and the relatively slow build-up of equally pure, nearly theoretically dense material, is the most practical approach. The general procedure in the case of silicon nitride consists of passing a mixture of vapor-borne precursors into a chamber, hot wall or cold wall, within which the precursors react and form deposition species. These then adhere to the heated substrate and crystallize. The process is continued until desired thicknesses are achieved. The chemistry and detailed transformation processes (deammination, crystal growth, etc.) involved in formation of deposits of certain characteristics are at present inferred primarily through analysis of the materials and correlation with the deposition conditions (temperature, pressure, gas feed rate and concentration, gas flow dynamics, substrate characteristics, etc.).

Silicon nitride can be formed from the vapor phase by interaction of ammonia and a silicon halide (e.g., silicon tetrachloride, -fluoride or-bromide), a silane derivative (e.g., chlorosilane SiH_xCl_y $(x + y = 4)$, or silane itself (SiH_4). Typical gross reactions are:

5.

$$3\ SiCl_4 + 4NH_3 \longrightarrow Si_3N_4 + 12\ HCl$$
$$3\ SiF_4 + 4NH_3 \longrightarrow Si_3N_4 + 12\ HF$$
$$3\ SiH_4 + 4NH_3 \longrightarrow Si_3N_4 + 12\ H_2$$

The interaction of silicon tetrachloride with ammonia has been the subject of systematic, detailed study for a number of years.[6,7] A series of solid intermediate complexes, which may be generally termed silyl imides, form immediately on mixing the two reagents in the vapor as well as liquid phase. Intermediates of this general type are believed to constitute the deposition precursors since they lose ammonia as a function of temperature to yield non-crystalline silicon nitride at temperatures around $1000^{\circ}C$.[7] Various sequences have been proposed to represent the course of these reactions. For example, Billy[6] has substantiated the following sequence by careful analysis:

$$SiCl_4 + 6NH_3 \longrightarrow SiN_2H_2 + 4NH_4Cl$$
$$2SiN_2H_2 \longrightarrow NH_3 + Si_2N_3H$$
$$Si_2N_3H + NH_4Cl \longrightarrow NH_3 + Si_2N_3H_2Cl$$
$$3Si_2N_3H_2Cl \longrightarrow NH_4Cl + 2Si_3N_4HCl \longrightarrow 2Si_3N_4 + 2HCl$$
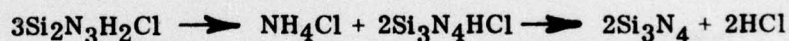
Formation of three dimensional polymeric species at lower temperatures which may be cyclic, and based on the monomer (SiN_2H_2), is also suggested by Billy[8] and may account for varying crystallite sizes or random large crystals in certain deposits. The precise composition and stoichiometry of the intermediate mixture in vapor deposition and the rates at which the various components form and decompose are undoubtedly of importance in determining the deposition rate, morphology and characteristics of a deposit formed under specific conditions of gas feed stoichiometry, concentration, mass flow rate, temperature and pressure. It would be reasonable to assume that the use of a hot wall versus a cold wall reactor would have an important influence on these factors simply by virtue of the different time-temperature profiles which the reactive mixture experiences en route to the substrate.

The chemistry of the silicon tetrafluoride-ammonia system has not been as well studied as that of the chloride system, although it has been reported to

6.

be considerably different.[9] Thus, the complex intermediate structures proposed by Billy and others for the chloride system may not be involved in the reaction sequence. The lower stability of ammonium fluoride would also ease the problem of byproduct accumulation.

The silane-ammonia system has not been reported to have yielded crystalline deposits at reasonable deposition rates, owing probably to the low thermal stability of silane itself. Airey, Clarke, and Popper have reported[10] that coherent deposits were not formed owing to premature formation of silicon in the vapor phase. Cochet, Mellottee and Delbourgo[11] analyzed the course of decomposition of a silane/ammonia mixture approaching a substrate heated to 950°C and concluded that the silane was completely decomposed in the gas phase. Thus, they claim that formation of silicon nitride would not be expected at the surface. At higher surface temperatures where crystalline deposits occur, decomposition even further into the gas phase would be expected with the loss of particulate silicon nitride particles except for accidental impingement on the substrate. This, however, is not very dissimilar to the chloride process in which intermediate silyl imide compounds are also formed although from more rather than less complex species. Decomposition also occurs in the gas phase, with deposition of crystalline material through impingement on a heated substrate. However, the lower temperatures at which the hydride process is conventionally carried out leads to the possibility of entrapment of incompletely decomposed intermediates such as $Si(NH)_2$, $Si_2(NH)_3$, etc., in the deposit with insufficient time and thermal energy for complete decomposition and crystal growth. The generation of too high a vapor-borne content of silicon nitride particles at temperatures below about 1350°C where crystal formation occurs could thus lead to sooting or formation of non-coherent deposits such as Airey, et.al., observed.[10]

In all of these chemical systems, formation of solid deposition precursors in the gas phase presents a somewhat different picture from processes in which deposition occurs when the vapor pressure of a nucleus in the boundary layer adjacent to the substrate exceeds the equilibrium value and precipitation occurs,

(e.g., gas phase supersaturation in the C-H system). In the latter case, removal of the depositing species leads to diffusion of more of the precursor molecules into the boundary layer as a result of the concentration gradient established. The silicon nitride deposition process might also be expected to be different from processes in which two species are reduced at the surface, at which location they interact to form a more thermodynamically stable compound, such as titanium boride (TiB_2), for example. The silicon nitride intermediates may undergo deammination in the gas phase, growing by collision until they either pass out of the hot zone, or impinge on a heated surface. At intermediate deposition temperatures, mixtures of both crystalline and vitreous silicon nitride are obtained, suggesting such a growth process. [12]

Therefore, in developing a practical process for formation of silicon nitride of optical quality, attention must be paid to the internal geometry of the deposition system, particularly if shaped parts are to be formed. Maximum opportunity for substrate contact should be provided under circumstances where clogging in the hot zone cannot occur through excessive vapor phase agglomeration. In all of the above chemical systems, removal of non-gaseous precursors will reduce the yield and may also cause clogging of the furnace lines, even in the absence of excess ammonia and ammonium chloride formation.

Table 2 is a summary of deposition conditions reported for deposition of silicon nitride from various chemical systems. In this work, an attempt was made to evaluate the three most common Si precursors in conjunction with NH_3, eventually focussing on one particular system for further optimization.

Table 2. Summary of CVD Si_3N_4 Research by Various Investigators

	Nilhara & Hirai(14)	Airey, Clarke and Popper(10)	Galasso(15) United Aircraft(16)	Gebhardt, Tanzilli and Harris(12)	Kijima, Setaka & Tanaka(17)	This Work
Si Feed (cc/min)	156 (SiCl₄)	30 (SiH₄) 42 (SiCl₄)	538 (SiF₄)	155 (SiF₄) 518 (SiCl₄)	6 (SiCl₄)	385-410 (SiF₄) 2.5-7.5 (SiH₄) 120-480 (SiCl₄)
NH₃ Feed (cc/min)	60	480-960 (tot. N)	2151	530-1050	---	60-3200
H₂ Feed (cc/min)	700	---	---	---	2000 (H₂ - N₂)	500-2650
N/Si Feed Ratio	0.38	1-15	4	6-15	1-3	0.5-640
Temp. Range (°C)	1100-1550	800-1200	1450	1100-1550	1600-1700	1400-1510
Press. Range (torr)	5-300	760	8.3	1-10	760	0.5-10
Reactor Type	CW	CW, HW	HW	HW	CW	HW
Substrate Size (cm)	2.5 x 4 x 0.2 Plate	4 x 3 x 0.2 Plate	8.3 x 8.3 Plate	1.3 x 1.3 x 20 Channel	--- Plate	10 dia. x 25 hi (see text)
Deposition Rate (mm/hr)	0.05-0.7	0.005-.035	0.125	0.1-0.25	Low	0.008-.64

9.

SECTION III

EXPERIMENTAL PROCEDURE

Deposition of silicon nitride from a variety of precursor silicon sources was carried out using a low pressure hot wall reactor (isothermal furnace) which has a hot zone of 10 cm. diameter x 25 cm high. A smaller furnace (2.5 cm dia. x 20 cm long) has also been used for a few runs. The heating element design in both furnaces provides a constant temperature along the element wall, which in turn heats a deposition chamber principally by radiation. Temperature variations within the deposition chamber are limited to those produced by losses from the chamber itself due to the gas flow, rather than element end losses which might occur in a furnace of different design. In this manner, the reagent gases do not pass through a temperature gradient of any considerable length, but should achieve equilibrium relatively quickly. The furnace is equipped with conventional gas handling facilities such as mass flowmeters, cold traps and a vacuum pump of high capacity compared to the usual gas feed rates associated with low pressure chemical vapor deposition. Temperatures are measured by optical pyrometer, while pressure is controlled by a nitrogen ballast valve at the pump.

Silicon tetrachloride of two grades was used: technical grade (Fisher Scientific) and electronic grade (Synthatron, Inc.). Silicon tetrafluoride was obtained from Matheson Co. and Synthatron - both were listed as being 99.6% pure. Ammonia was 99.0% pure (Matheson), pumped from the liquid, as were the silicon precursors. Hydrogen (Airco) was reported to be technical grade (dew point: -67.8°C or $\sim$ 3.5 ppm H_2O). Hastings-Raydist mass flowmeters were used to meter the vapors into the furnace with calibration curves based on literature values of specific heats of the materials. Total mass of $SiCl_4$ fed was determined by weighing the feed cylinder before and after an experiment and comparing the difference to the mass fed as calculated from flowmeter readings. There is some disagreement in this area which is believed to have been caused by uneven distillation or boiling

10.

of the liquids in the feed cylinder. Heating was provided to offset the decrease in feed cylinder temperature caused by evaporation. Based on analysis of the deposits, however, there does not appear to be evidence that variations in feed stoichiometry were responsible for effects such as banding or sooting. Formation of nodules, however, may result from this in the chloride system. These were not observed in the fluoride system.

Silane was obtained as a three percent mixture in nitrogen (Matheson) and was metered to the furnace through a mass flowmeter.

After passing through the reaction zone, the gaseous materials were pumped through liquid nitrogen traps and into a purged vent line.

Following deposition, the furnace assembly was cut apart and the deposit removed from the graphite substrate by heating in air at $817^\circ C$ for a sufficiently long period to remove all traces of graphite. In certain cases, a thin pyrolytic graphite layer was deposited on the substrates to ease the residual stresses in the deposit, to obtain a smoother backface and to prevent carbon contamination. It is believed that this also provided some degree of protection against the attack of polycrystalline graphite by ammonia.

In the deposition studies performed on this program, several geometries were evaluated for the purpose of achieving reasonable deposition rates as well as for forming flat and shaped materials. In general, larger open cross-sections resulted in lower rates, with concomitant plugging of gas exhaust lines with undecomposed intermediate deposits. This tended to limit deposition times at constant pressure, and geometries were accordingly modified to offset this effect. In addition to the problem of clogging induced by loss of intermediates, unreacted ammonia in the feed mixture contributed to clogging through formation of solid ammonium chloride by reaction with the HCl gas released by reduction of the silicon tetrachloride.

11.

SECTION IV

EXPERIMENTAL RESULTS AND DISCUSSION

4.1 Process Development

Table 3 summarizes the process conditions used in these studies. The majority of the runs were performed in the larger furnace mentioned above, using various geometries to maximize yield and reduce clogging. (See Section 4.1.1). Some were performed using the smaller furnace with a channel geometry. In general, deposition runs involving the use of silicon tetrachloride and ammonia were terminated prematurely because of plugging of furnace lines a) when the ammonia/silicon source ratio was high, and b) when the furnace geometry had a large open cross-section. Unlike the cold wall reactor systems, the hot wall system in use here offers little opportunity for collection of unreacted species which are not converted on contact with the substrate. Thus, the geometry of the internal deposition zone is important - deposition runs in which the gas stream had ample opportunity to contact hot surfaces produced considerably less unreacted byproducts and usually presented no plugging problems. Less trouble was also encountered with the fluoride system than with the chloride system, and there was no difficulty with the silane system other than the low deposition rates due to the low concentration of silane available with the dilute gas mixtures used. These observations are in line with the degree of conversion of the silicon precursor to deposited silicon nitride.

The deposits ranged from black to white, finely crystalline to heavily and coarsely nodular. The fluoride deposits were also much finer grained than the chloride, and had a considerably lower tendency to form nodules and large faceted crystals. This could be attributed to the occurrence of fewer (if any) intermediate species particles of significant size in the fluoride system.

Niihara and Hirai[13] relate the lightest colors with the highest levels of oxygen contamination; work conducted at GE-RESD on IR&D funding, however, shows that addition of metallic elements such as aluminum or niobium also influences color, other things being equal. Niihara and Hirai[14] have also

Table 3. Experimental Conditions for Deposition of α-Si$_3$N$_4$

Run No.	Si Precursor	Substrate Material	Geometry	Feed Rate (cc/min.)				N/Si Ratio	Furnace Press. (torr)	Temp. (°C)	Dep. Rate (mm/hr)	% Si Conv.
				SiX$_4$	NH$_3$	H$_2$	N$_2$					
1	SiCl$_4$	PG	Inv. Dome	240	3000	--	--	12.5	5-10.5	1500	.20	42.7
2.	SiCl$_4$	PG	Inv. Dome	480	3200	--	--	6.7	5-10	1500	.53	40.3
3.	SiCl$_4$	PG	Dome Plate	480	640	2650		1.3	9.5	1510	.23-.51	80.3
4.	SiCl$_4$	Grafoil	Channel	120	60	700		0.5	10	1450	.33	10.6
5.	SiH$_4$ 3%/N$_2$	Grafoil	Box	2.5	800		400	640	2.0	1450	.005	--
6.	SiH$_4$ 3%/N$_2$	Grafoil	Channel	7.5	350		500	180	0.5	1400	.010	--
7.	SiF$_4$	PG	Plate Flow	385	350	500		0.9	3.5-6	1425	.025-.04	13.5
8.	SiCl$_4$	PG	Plate Flow	360	470	2650		1.3	5	1500	--	100.0
9.	SiCl$_4$	Graphite	Plate Flow	360	470	2650		1.3	5-6	1500	.64	51.0
10.	SiF$_4$	Graphite	Plate Flow	480	350	500		0.7	10	1450	.10	21.7

correlated the morphology of the deposits with respect to temperature and pressure of formation and with the location of feed material emerging from a cold reactor inlet tube and impinging directly on the heated substrate.

Deposits made on Grafoil Ⓡ and pyrolytic graphite surfaces had a tendency to curl, particularly at the higher temperatures (ca. 1500°C). This appeared to have occurred early in the course of a run, since the edges of curled sections were coated. This may have resulted from peeling of the substrate layer (pyrolytic graphite or Grafoil Ⓡ) from the polycrystalline substrates, particularly as broad flat plates caused cracking of deposits at the upper and lower ends, where deposit thickness was low. At lower temperatures (1400-1450°C), curling was less of a problem. No deposition runs were made at low temperatures where vitreous deposits are normally encountered, e.g., below 1300-1350°C, since the interest in this first year program was related to crystalline properties.

4.1.1 As-Deposited Configurations

Several mandrel designs were used for preparing "thick", free-standing deposits of crystalline Si_3N_4. A summary of these are listed below:

(1) flat-plate and dome mandrels oriented normal to the flow positioned within a deposition tube of circular cross-section (e.g., Run Nos. 1, 2, 7).

(2) dual purpose mandrel for forming both flat plate and dome configurations simultaneously (Run No. 3).

(3) flat-plate mandrels oriented both normal or parallel to the flow positioned within deposition tubes of hexagonal cross-section (e.g., Run Nos. 8,9).

(4) deposition tubes of circular outside diameter and rectangular cross-sectional area on the inside (typical of that used in the smaller diameter 2.54 cm furnace, e.g., Run Nos. 4 and 6).

The following post-deposition photographs illustrate some of the mandrel configurations used for forming monolithic α-Si_3N_4.

Figure 1 illustrates a dome mandrel showing both the first and last deposited surface. The dome was subsequently ground and polished for optical property evaluation. The formation of excessive nodular growths during the latter stages of deposition presented a major obstacle during grinding and polishing.

14.

(a) Last Deposited Surface

$$
\begin{array}{ccccc}
\mid & \mid & \mid & \mid & \mid \\
0 & 1 & 2 & 3 & 4
\end{array}
$$
cm
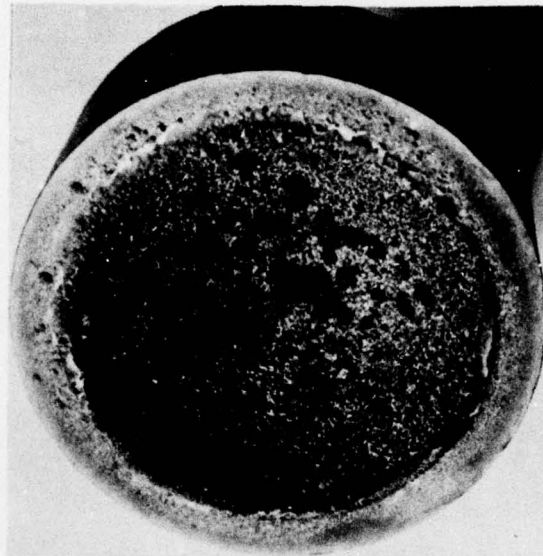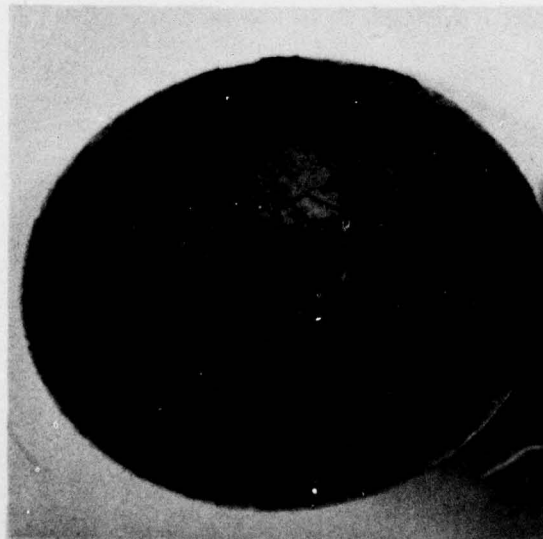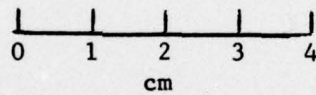
(b) First Deposited Surface

Figure 1. Dome Mandrel (a) Showing Last Deposited Surface and
(b) First Deposited Surface After Removal of Graphite
Substrate. Run No. 1.

Figure 2 shows a dual purpose mandrel used for forming both flat-plate and dome configurations simultaneously. Nodular overgrowths were again obtained during the latter stages of deposition. In order to increase the yield of flat plate material, an inner deposition tube with a hexagonal cross-section was positioned within the normal cylindrical deposition tube. Figure 3 shows the six side plates removed after a deposition, and also a flat plate mandrel of hexagonal cross-section which was oriented normal to the flow during the experiment. Excessive nodular growth occurred during the latter stages of deposition. The most successful mandrel design for forming flat plate material consisted of two parallel rectangular deposition plates oriented parallel to the flow. Figure 4 shows two typical plates which were positioned within a deposition tube with a hexagonal cross-section. Experiments conducted in the smaller 2.54 cm diameter furnace utilized a flat plate mandrel formed as an integral part of a deposition tube of circular outside diameter with a rectangular channel forming the inside contour. Figure 5 shows a longitudinally sectioned deposition tube, and also the inlet nozzle tube through which feed gases were mixed prior to entry into the deposition channel.

4.2 Physical Property Characterization

4.2.1 Microstructure

4.2.1.1 X-Ray Diffraction

Preferred orientation of crystalline α-Si_3N_4 deposits varied from almost random (Run No. 3) to highly preferred (Run Nos. 9 and 10). Figures 6, 7 and 8 illustrate the actual measured diffraction data obtained from polished surfaces (both sides) of each material. In all cases, differences in preferred orientations were observed between front and back surfaces of polished specimens.

4.2.1.2 Scanning Electron Microscopy

Figures 9, 10 and 11 show typical last deposited surface morphologies for the three precursor reactant types studied. For Run No. 10 (Figure 11), a range of morphologies were observed varying (a) from a mixture of faceted and nodular crystallites to (b) an exclusively nodular growth pattern with growth cone diameters approximately three times that observed in the mixed growth region. This particular deposition run was also unusual in that amorphous zones were detected

16.
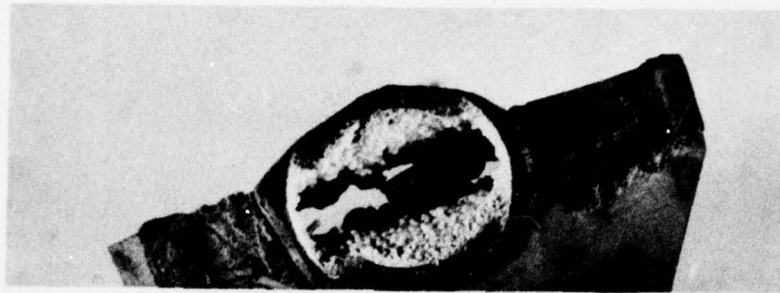
(a) Inlet Port

Flow
Direction
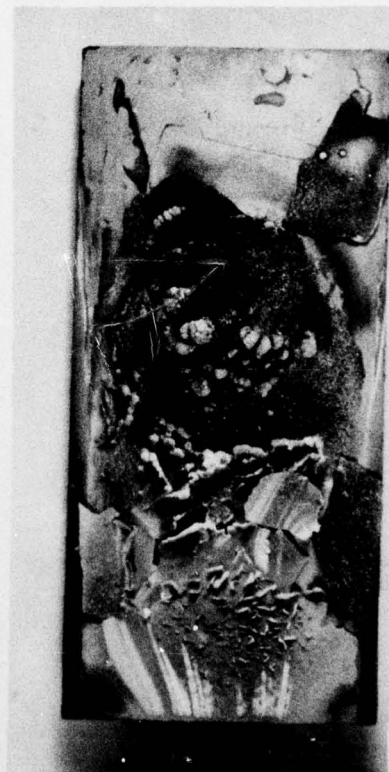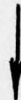
(b) Female Mandrel

(c) Male Mandrel

Figure 2. Dual Purpose Mandrel for Forming Both Flat-Plate and
Dome Configurations Simultaneously. A Rectangular
Flow Channel Was Formed By Combining the (b) and (c)
Portions of the Mandrel. Also Shown is Assembled
Mandrel Showing Gas Inlet Port to Internal Mandrel
Cavity. Run No. 3.

17.

Flow
Direction

0 2 4 6 8 10
cm
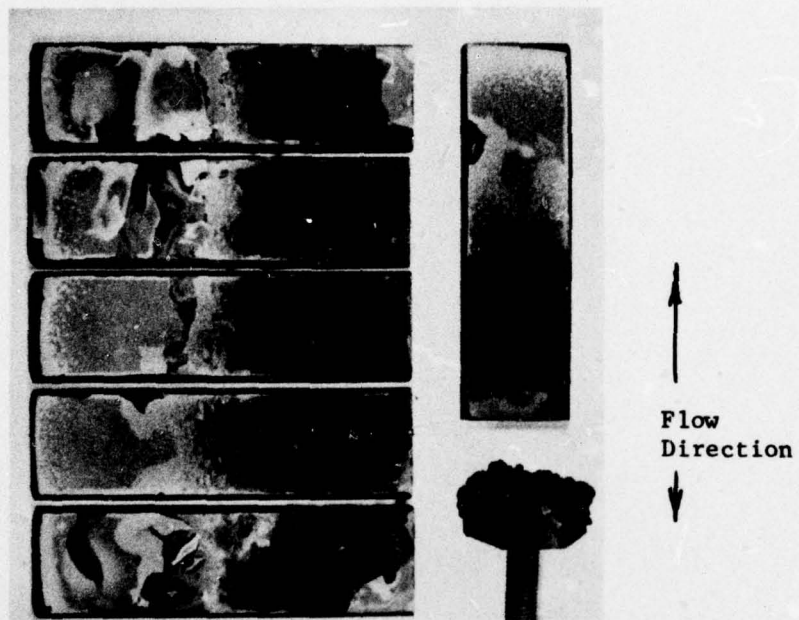
Figure 3. Flat Plate Mandrel of Hexagonal Cross Section Oriented
Normal to Flow. Also Shown are Six Flat Plates Which
Formed the Sides of the Corresponding Deposition Tube
With a Hexagonal Cross-Section. Excessive Nodular Growth
Occurred Both on the Side Plates and Hexagonal Flat-Plate
Pedestal. Run No. 8.

18.

Direction
of
Flow
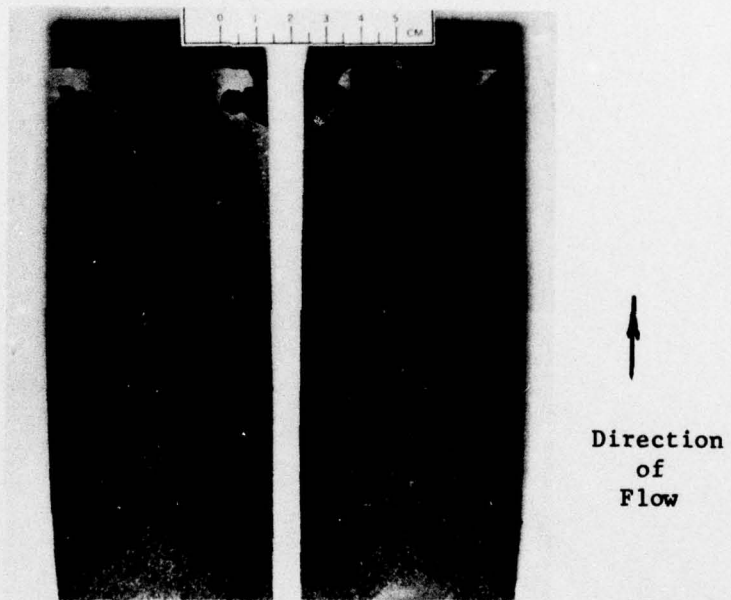
Figure 4. Flat Plate Mandrel Aligned With Flow. Two Parallel
Plates Shown Were Suspended in a Deposition Tube
With a Hexagonal Cross Section. Run No. 9.
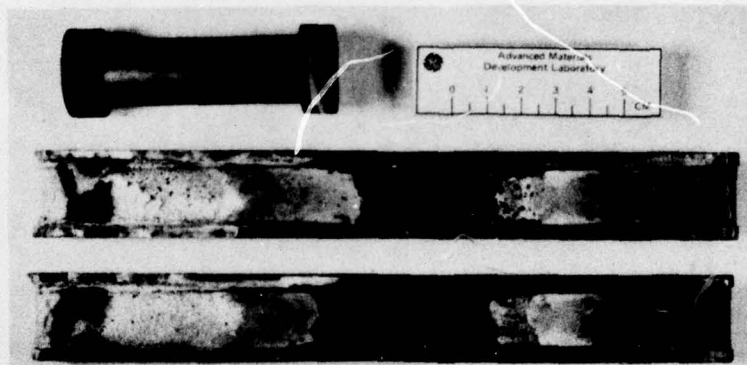
Figure 5. Flat Plate Mandrel Formed As Part of a Deposition Tube
of Circular Outside Diameter With a Rectangular Cross-
Sectional Area on the Inside Contour. Photograph Shows
the Inlet Nozzle and Longitudinally Sectioned Deposition
Tube. Run No. 6.
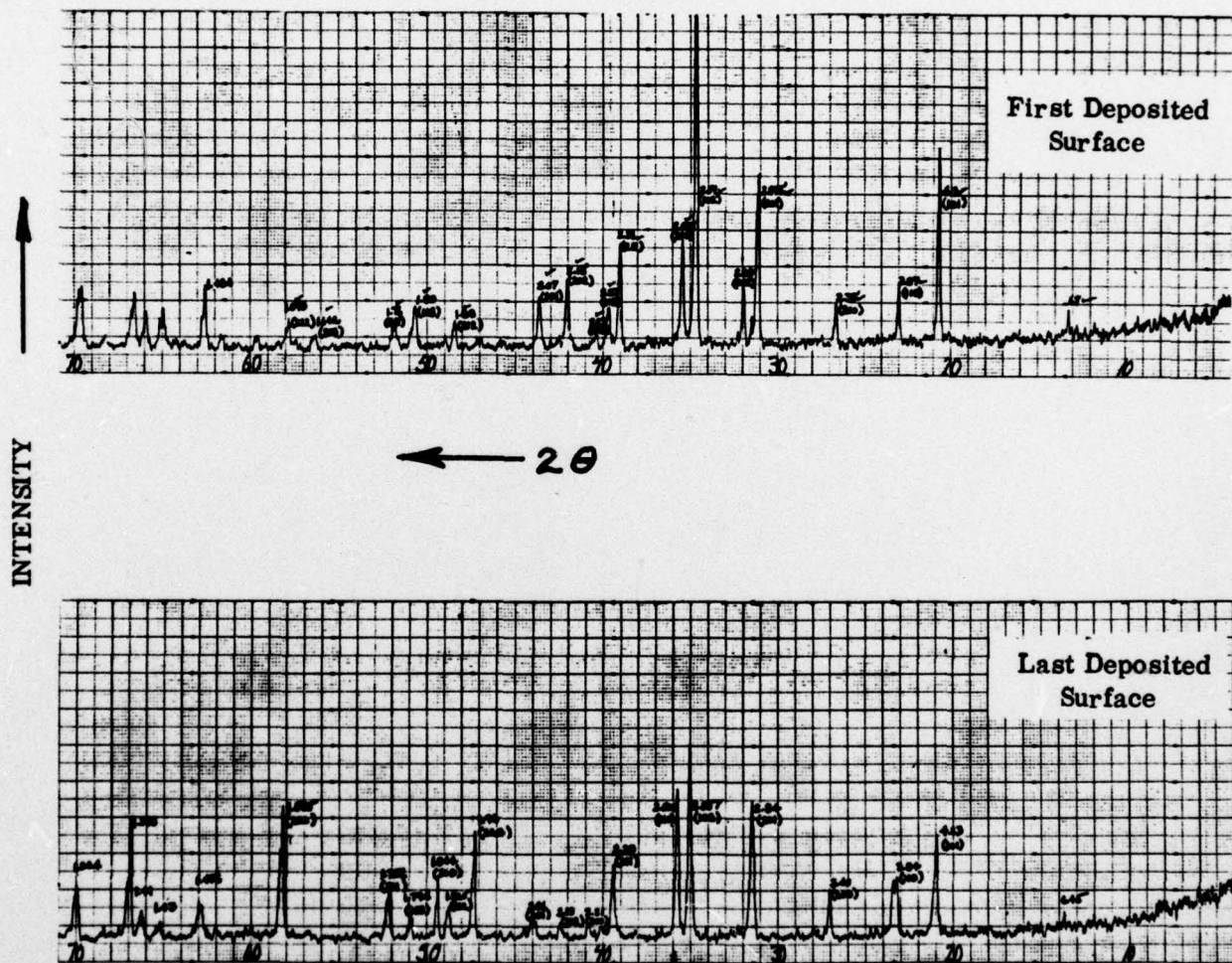
Figure 6. X-Ray Diffraction Scans of Polished α-Si$_3$N$_4$ Plate Extracted From Run No. 3.

21.
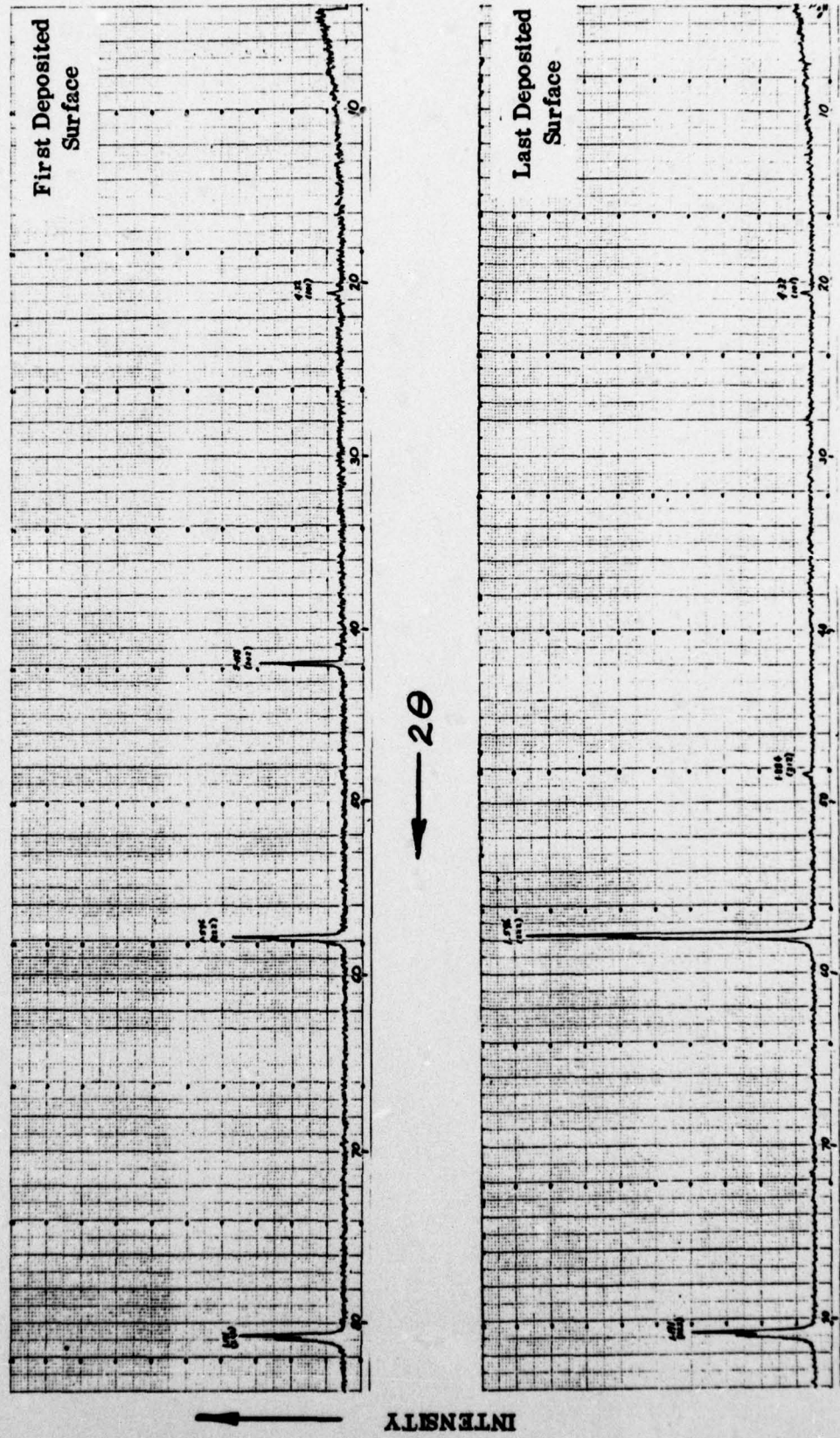
Figure 7. X-Ray Diffraction Scans of Polished α-Si$_3$N$_4$ Flat Plate Extracted from Run No. 9.

22.
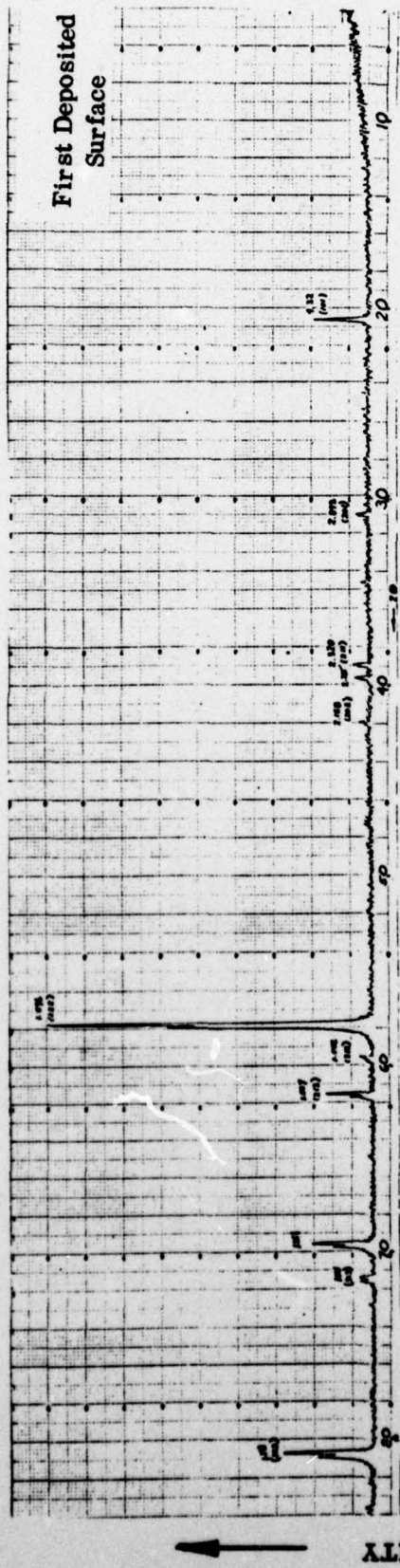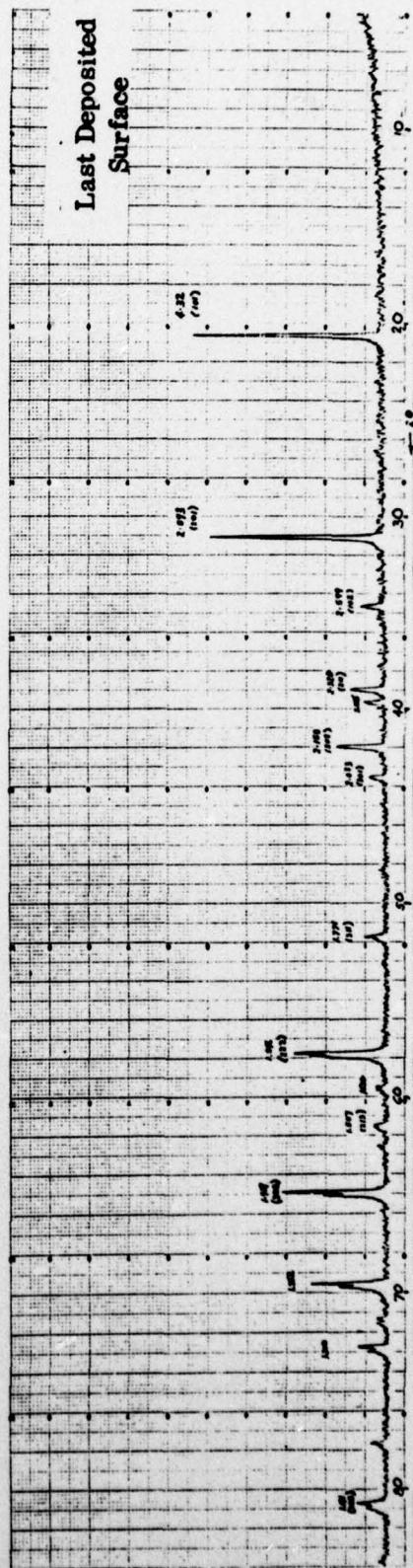
Figure 8. X-Ray Diffraction Scans of Polished α-Si$_3$N$_4$ Flat Plate Extracted From Run No. 10.

INTENSITY

23.
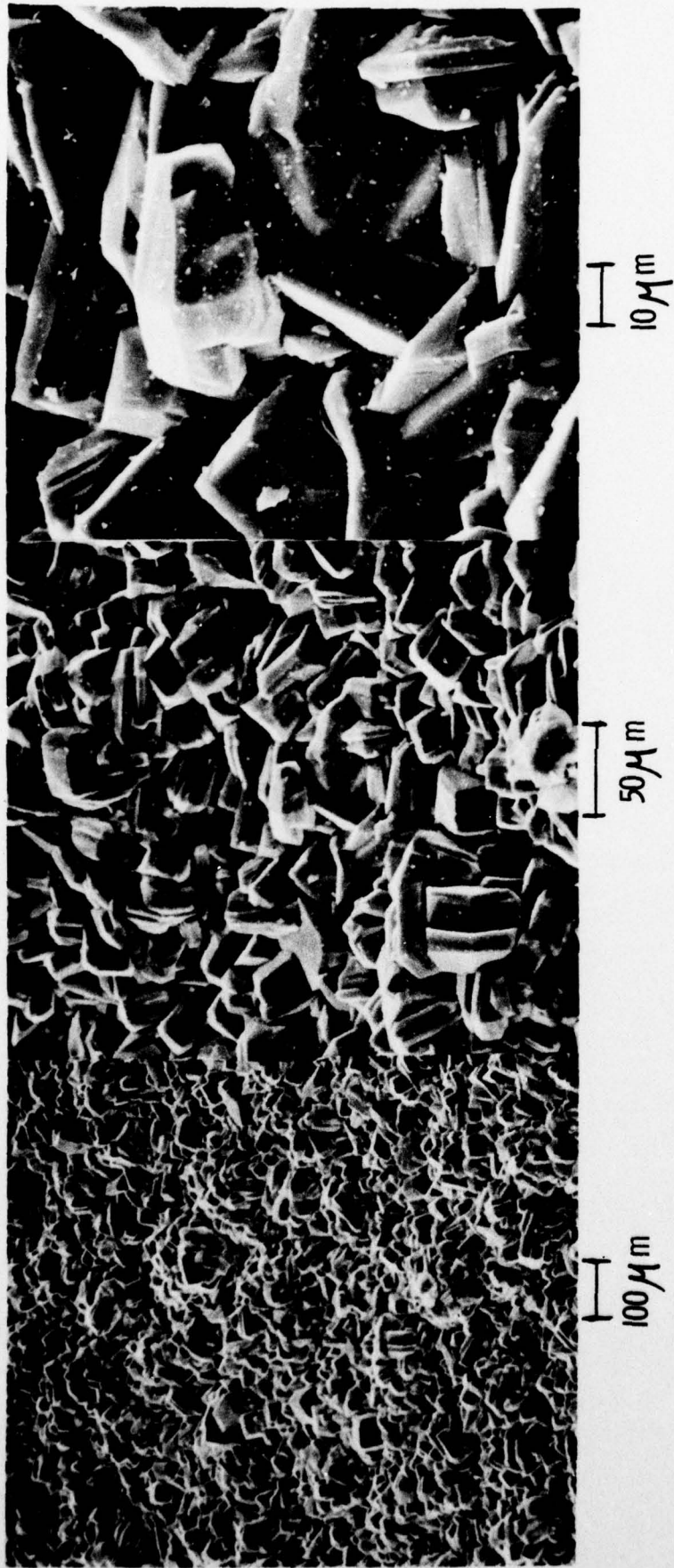
Figure 9. Last Deposited Surface Morphology of α-Si$_3$N$_4$ Deposited Using Silane/Ammonia Reactants (Run No. 5).

10 μm

50 μm

100 μm

24
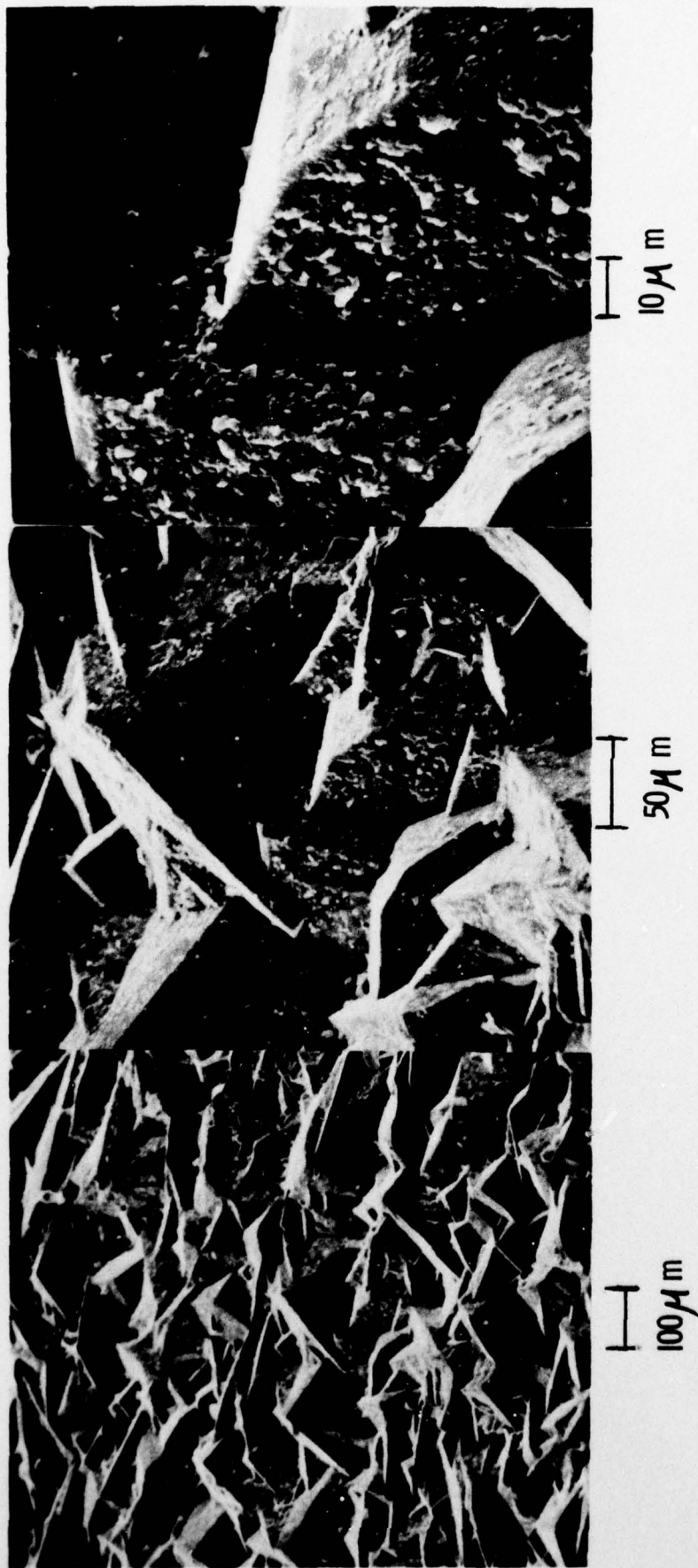
Figure 10. Last Deposited Surface Morphology of α-Si$_3$N$_4$ Deposited Using Silicon Tetrachloride/Ammonia Reactants (Run No. 9).

(a)

(b)

50 μm

100 μm

10 μm

50 μm

100 μm
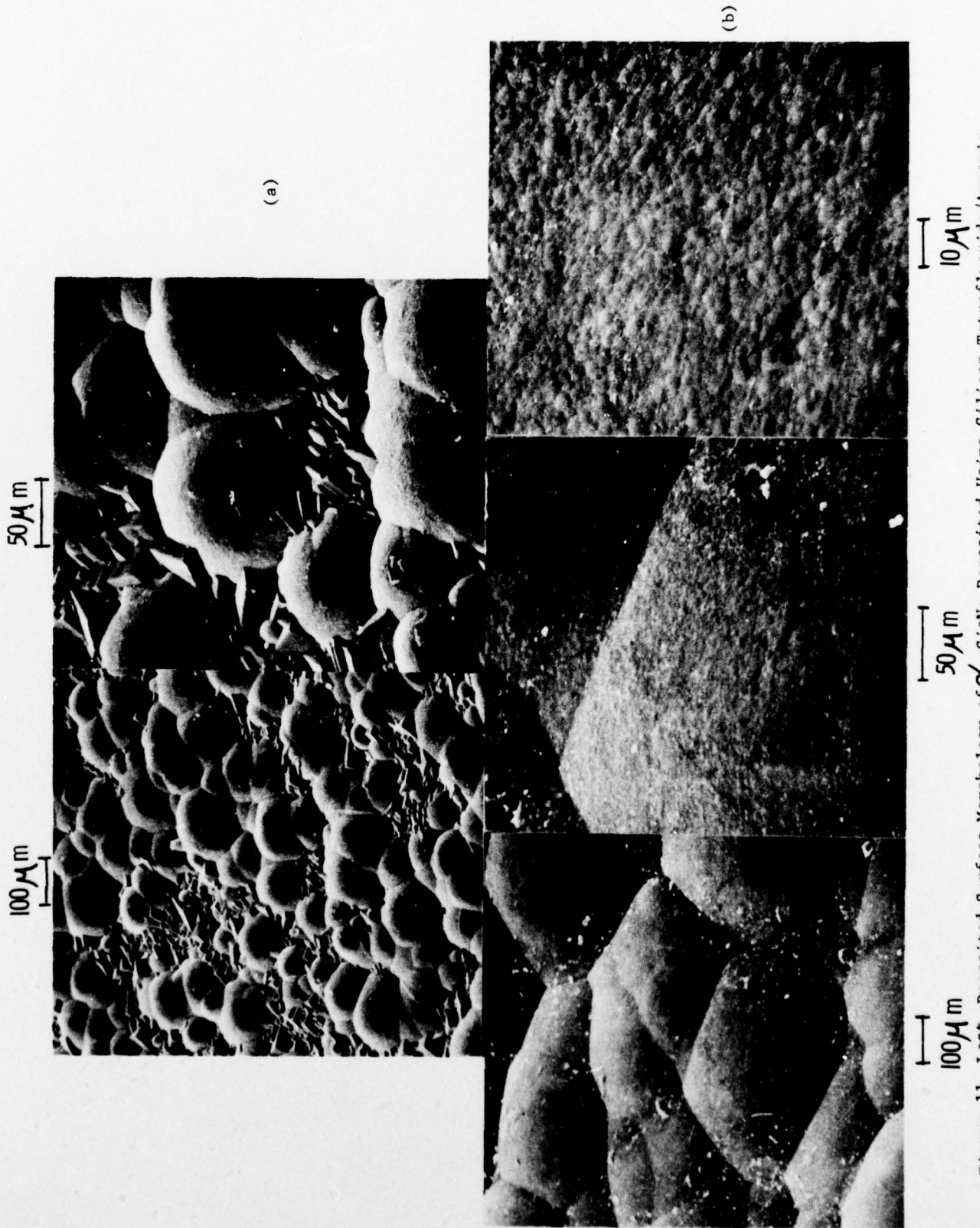
Figure 11. Last Deposited Surface Morphology of α-Si₃N₄ Deposited Using Silicon Tetrafluoride/Ammonia Reactants (Run No. 10).

within the depth of the deposit in regions selected for grinding and polishing. Flexure strength on typical material from this experiment was approximately one-third that observed for crystalline deposits with a faceted last deposited surface (Run No. 9). Also, the average Young's modulus for material from Run No. 10 was approximately one-half that observed for crystalline deposits with a faceted last deposited surface (Run No. 9).

4.2.1.3 Transmitted Light Microscopy

Figures 12 and 13 illustrate the microstructural characteristics of α - Si_3N_4 deposits as viewed in polarized transmitted light. The average grain size in the plane of the deposit varies from 2-30 microns for Run No. 9 to 40-60 microns for Run No. 10. The presence of a void structure is observed in the lower magnification photomicrographs of both deposits. Also, the presence of larger, isolated spherulitic grains are present in both deposits. These regions represent areas of high visible specular transmittance (i.e., good imaging capability).

4.2.2 Microhardness

Table 4 summarizes Knoop microhardness measurements using a 500 gram load. Although not determined in this study, Knoop microhardness values on brittle materials vary inversely with applied load.[18] For example, unpublished Knoop microhardness data on similar CVD α -Si_3N_4 deposits have been found to range from 3580 to 4240 Kg/mm^2 for a 100 gram load and correspondingly from 1600 to 1820 Kg/mm^2 for a 3000 gram load. It should be noted that Vickers hardness numbers would be approximately 30 percent higher than the Knoop microhardness measurements.

4.2.3 Mechanical Properties

Figure 14 shows the four point flexure strength fixture used for making room temperature flexure strength determinations. Strain gages were attached to specimens extracted from Run Nos. 9 and 10. A summary of flexure strength data including failure strain and modulus of elasticity is given in Table 5. The lower flexure strength and Young's modulus of material from Run No. 10 is attributed to non-typical microstructural development during deposition.

27.

100 μm
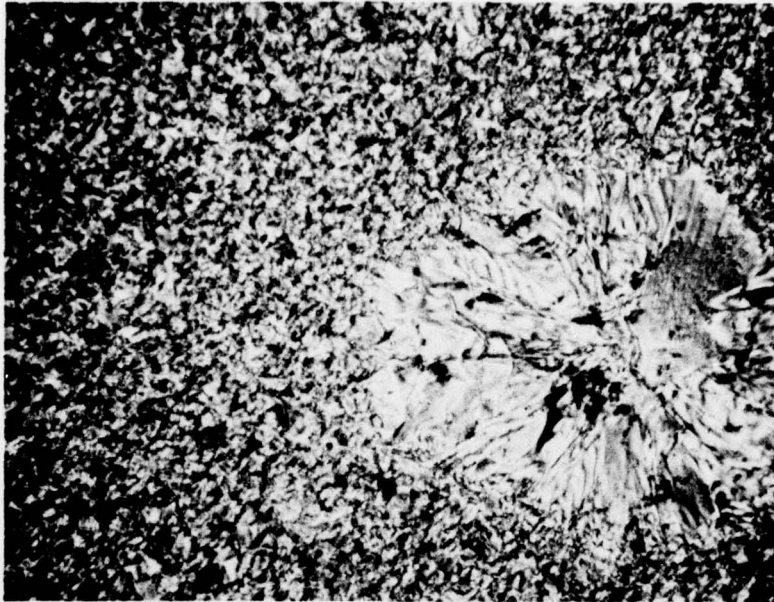
10 μm

Figure 12. Photomicrographs of Polished α-Si$_3$N$_4$ Viewed in Polarized Transmitted Light Parallel to the Deposition Plane. Run No. 9.

28.

100 μm
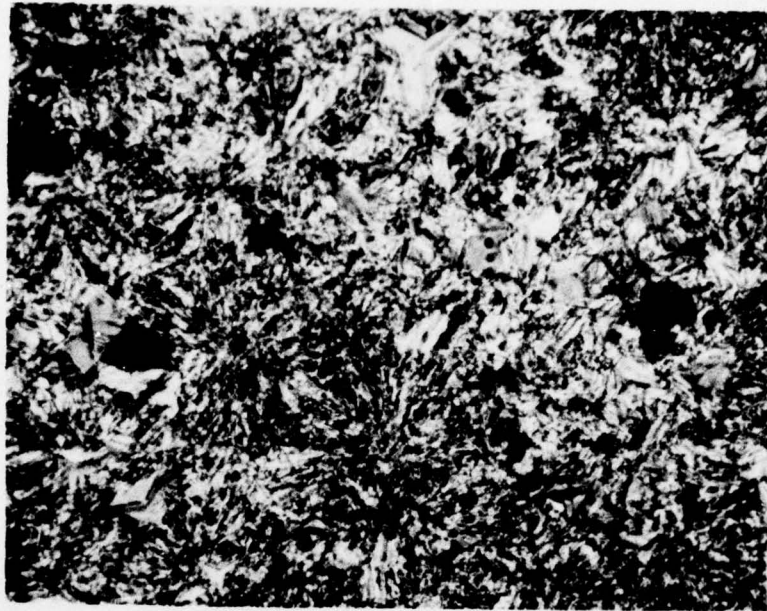
10 μm

Figure 13. Photomicrographs of Polished α-Si$_3$N$_4$ Viewed in Polarized Transmitted Light Parallel to the Deposition Plane. Run No. 10.

Table 4. Knoop Microhardness for CVD α-Si$_3$N$_4$

Run No.	Knoop Microhardness, kg/mm^2 *	
	Surface Parallel to Deposition Plane	Surface Normal to Deposition Plane
1	2351	2344, (2410) ***
2	2416	2365
3	2317	2326
4	2565	2479
5	2354, (1911) **	2196

*   500 g load, average of six readings

**   frosty region (partially amorphous and microcracked)

***   single crystal clear region
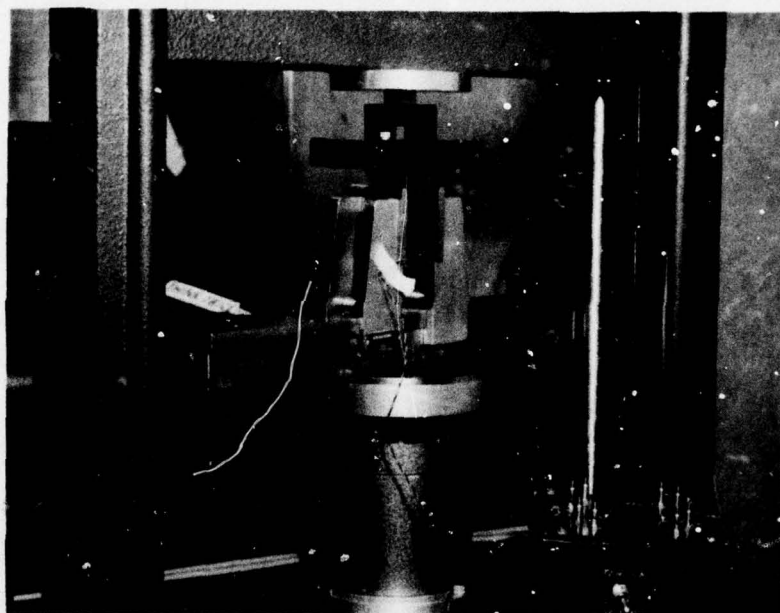
Figure 14. Four-Point Flexure Strength Fixture

Table 5. Flexure Properties of CVD α -Si$_3$N$_4$

Run No. 9	Flexure Strength		Failure Strain	Young's Modulus	
	MPa	psi	%	GPa	psi
	233.66	33880	0.07	334.48	48.5×10^6
	154.90	22460	0.05	311.72	45.2×10^6
	213.03	30890	0.07	297.52	43.14×10^6
	271.31	39340	0.09	304.90	44.21×10^6
$\overline{X}$	218.22	31642	0.07	312.14	45.26×10^6
Run No. 10	62.03	9140	0.03	206.90	30.00×10^6
	45.45	6590	0.03	131.72	19.10×10^6
	89.38	12960	0.06	203.86	29.56×10^6
	38.62	5600	0.04	132.41	19.20×10^6
	64.76	9390	0.03	203.66	29.53×10^6
$\overline{X}$	60.25	8736	0.04	175.72	25.48×10^6

Limited characterization of material from this experiment indicated that amorphous zones existed through the thickness at some locations. The Young's moduli recorded for material from Run No. 9 is typical of that recorded in the literature for hot-pressed β-Si$_3$N$_4$ indicating that this set of flexure strength is probably more typical of CVD α-Si$_3$N$_4$ at its current stage of development in our laboratory.

Subsequent three-point flexure strength measurements (4 specimens) by Freiman at NRL on material from Run No. 9 showed an average tensile strength of 164.09 MN/m^2 (23.8 kpsi) in the as-machined condition. Additional flexure specimens (4) were heat treated at 1430°C for 100 hrs. yielding an average room temperature flexure strength of 218.56 MN/m^2 (31.7 ksi). The fact that the strength did not decrease after this heat treatment is significant since over 50 percent drops in strength have been observed on commercial hot pressed Si$_3$N$_4$ after similar heat treatments.

4.2.4 Optical Properties

Spectral transmittance and reflectance properties of ground and polished deposits were obtained for several runs. In some instances, hemispherical as well as specular transmittance was measured to determine the degree of scattering in polished deposits.

4.2.4.1 Dome Configurations

Infrared transmittance properties for the first dome segment which was ground and polished is shown in Figure 15. Figure 16 shows similar transmittance data for a full dome segment which exhibited improved infrared absorption coefficients in the infrared. An estimate of projected transmittance properties for a dome segment of approximately half the thickness of the ground and polished dome is also shown. By applying an antireflecting coating, one may recover surface reflection losses estimated to be approximately 20 percent. The data shows that CVD α-Si$_3$N$_4$ when optimized may be utilized as a window with a transmittance cut-off of approximately 4.5 microns.

4.2.4.2 Plate Configurations

Figure 17 shows similar infrared transmittance data for a polished flat plate from Run No. 3 again confirming an infrared transmittance cut-off at
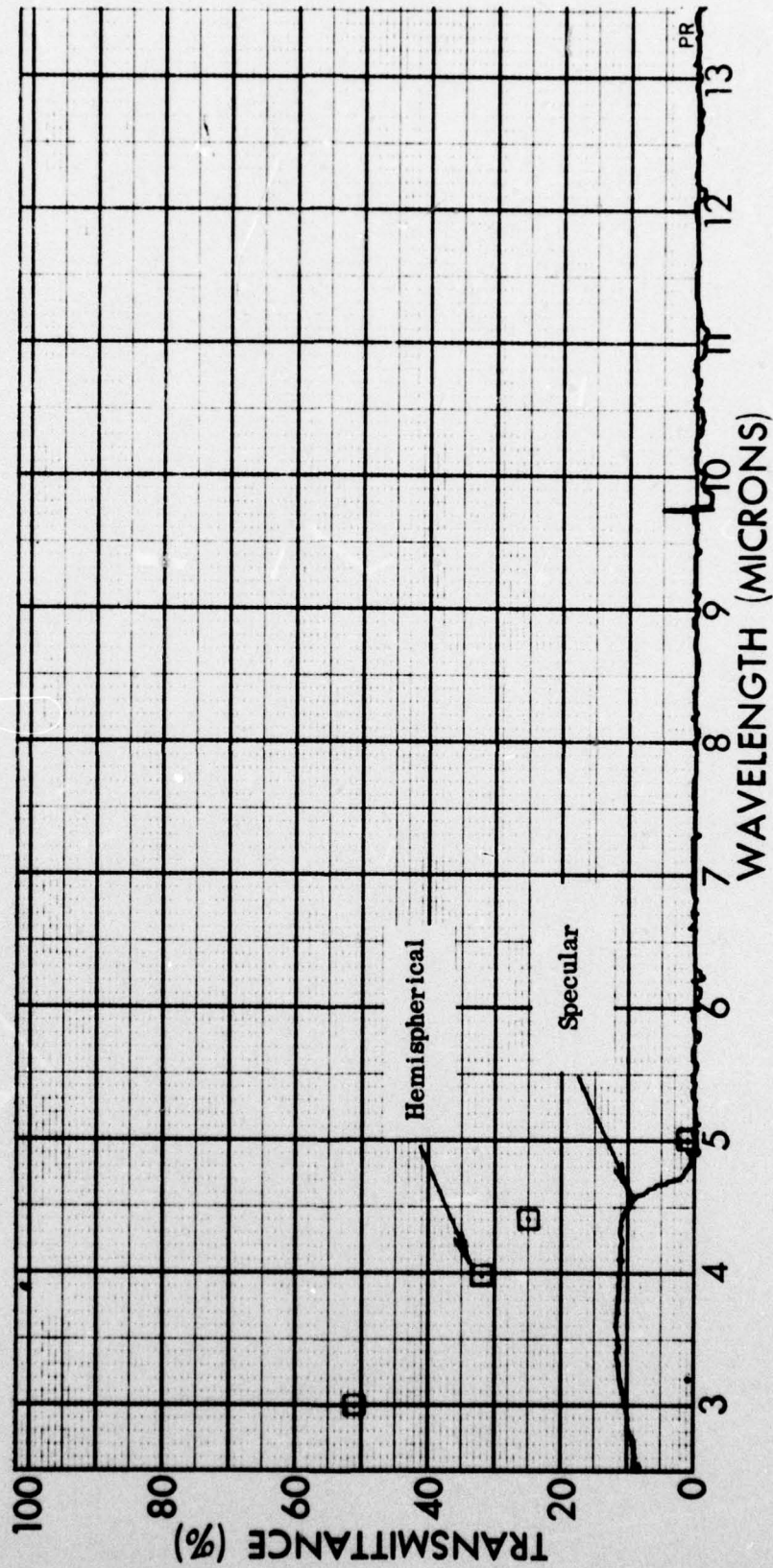
Figure 15. Specular and Hemispherical Transmittance of Polished Dome Segment of CVD α- Si_3N_4. Run No. 1. Specimen Thickness = 1.651mm

34.
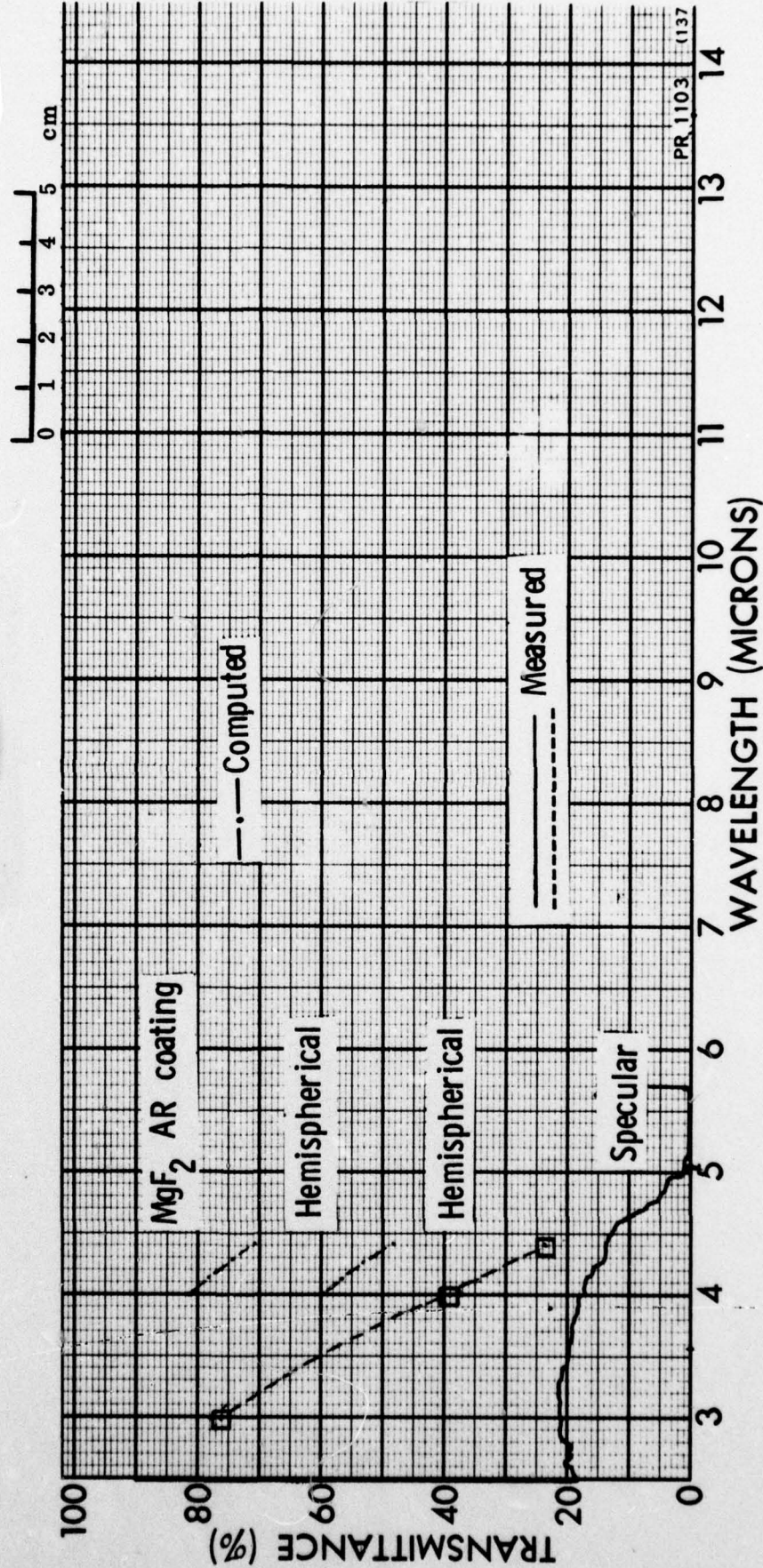
Figure 16. Specular and Hemispherical Transmittance of a Polished Dome of CVD α-Si$_3$N$_4$ (Photograph). Specimen Thickness = 2.261 mm. Estimate of Transmittance Properties with and without an Antireflecting Coating for a 0.927 mm Dome Also Plotted. Run No. 2.

35.
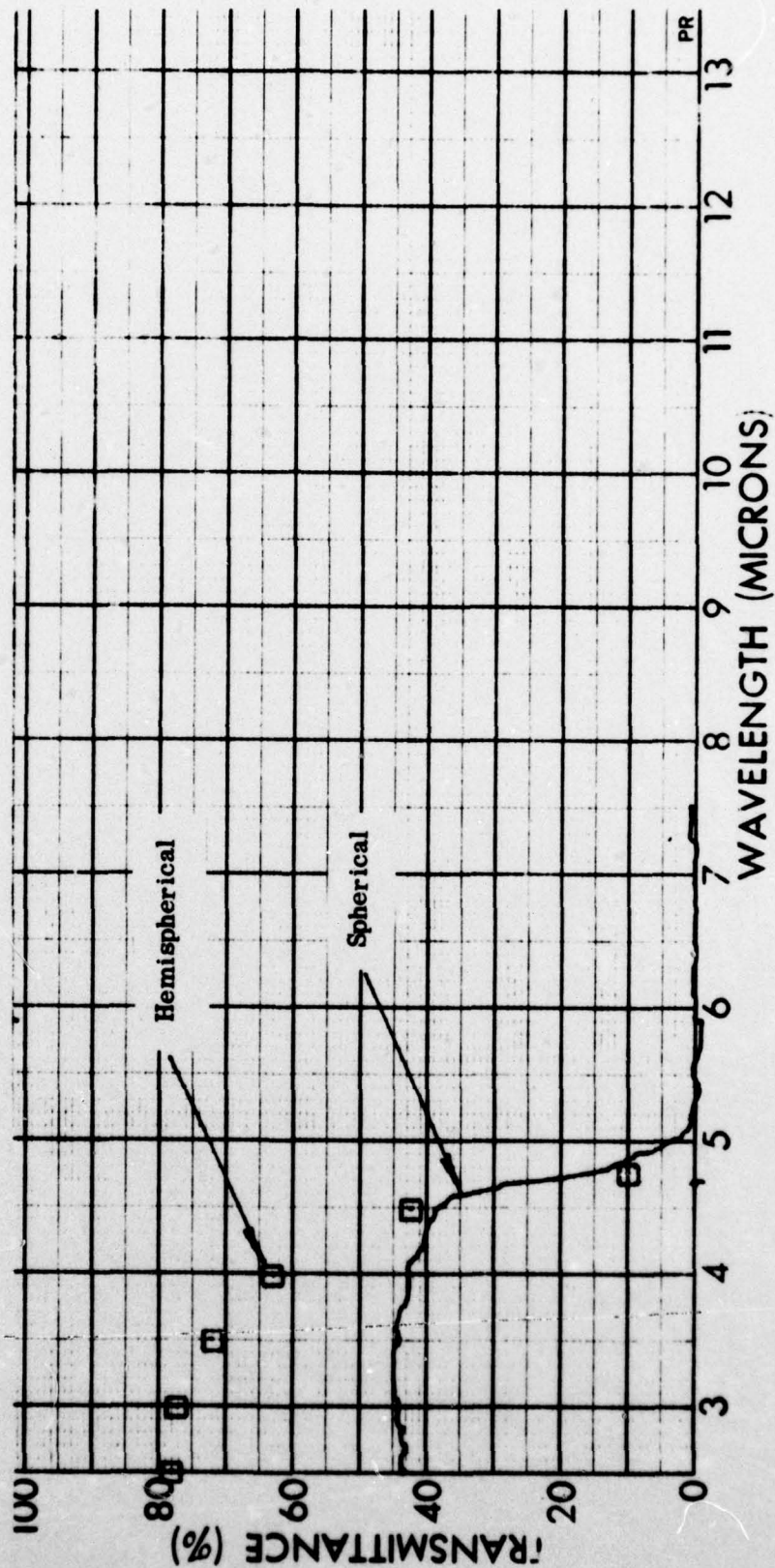
Figure 17. Specular and Hemispherical Transmittance of a Polished Flat Plate of CVD α-Si_3N_4. Run No. 3. Specimen Thickness = 0.747 mm.

36.

approximately 4.5 microns. The degree of scattering relative to the specular transmitted component is reduced as the transmittance cut-off wavelength is approached.

4.2.4.3 Visual Color Characteristics

Visual color variations have been observed within and between deposits synthesized in this study. Material from Run Nos. 9 and 10 are examples of the range of color variations observed, i.e., water-clear to dark amber. Figures 18 and 19 show the hemispherical and specular transmittance properties of material from each experiment. Although both deposits approach the 80 percent intrinsic transmittance limit in the near infrared wavelength region, significant transmittance differences exist in the ultraviolet and visible wavelength regions (0.30 to 0.7 microns). These color differences have been attributed to variations in oxygen content by Niihara and Hirai[13] with white material being associated with oxygen levels in excess of 1 weight percent. Figures 20 and 21 show the hemispherical and specular transmittance characteristics of both types of deposits in the infrared wavelength region. In this wavelength region, no transmittance differences are observed for either deposit. Also, the magnitude of the scattered transmittance component decreases beyond 3 microns. Correspondingly, the specular reflectance behavior of each type of deposit remains identical as shown in Figures 22 and 23.

4.2.5 Dielectric Properties

In order to accommodate the non-standard specimen geometries which could be extracted from flat plate deposits, a resonant cavity technique was developed patented after a method described in ASTM D2520-70, entitled "Complex Permittivity of Solid Electrical Insulating Materials at Microwave Frequencies and Temperatures to 1650°C." Figure 24 shows the laboratory set-up used for recording data from which the dielectric constant and loss tangent for CVD α-Si_3N_4 was computed. Table 6 summarizes dielectric data from Run Nos. 9 and 10. The loss tangent data for CVD α-Si_3N_4, being an order of magnitude lower than literature data on hot-pressed and reaction-sintered modifications of Si_3N_4, is especially noteworthy. If this trend continues at elevated temperatures,
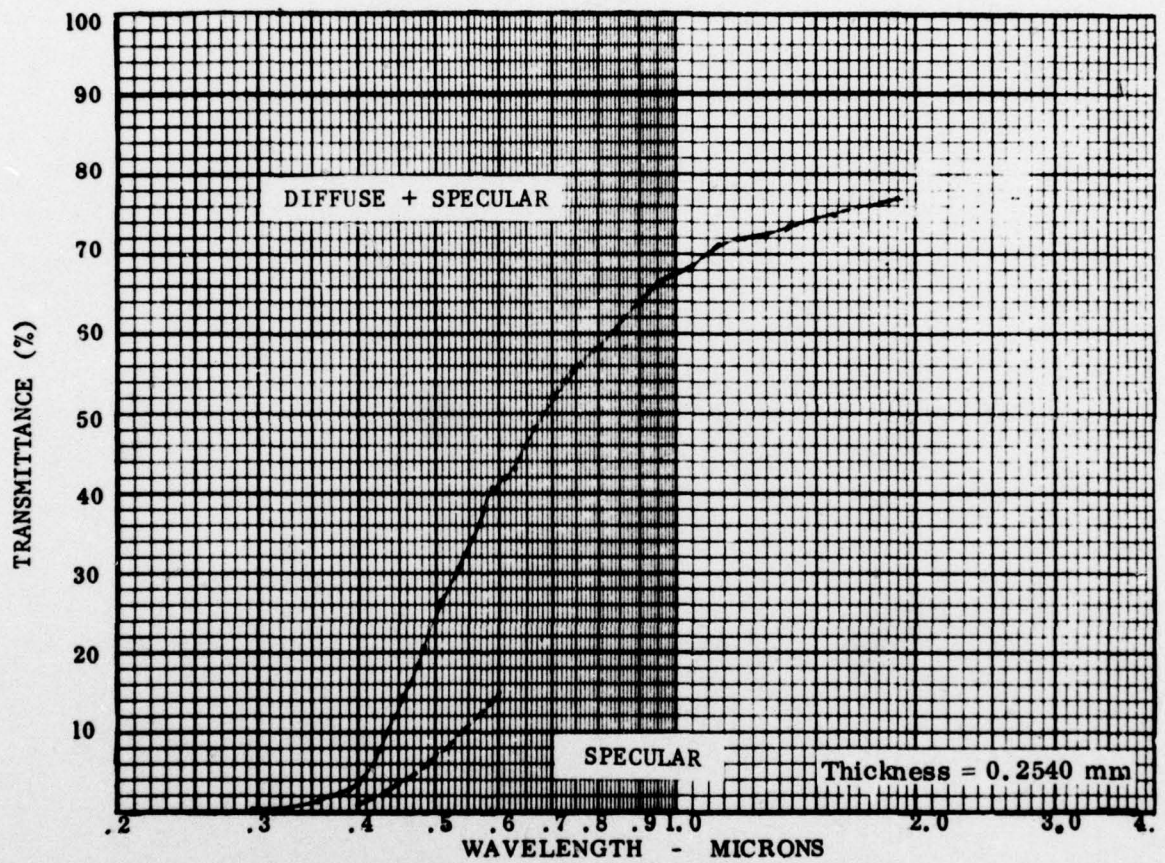
Figure 18. Hemispherical and Specular Visible Transmittance of Polished Flat-Plate α-Si$_3$N$_4$ from Run No. 9. Specimen Thickness = 0.2540 mm.
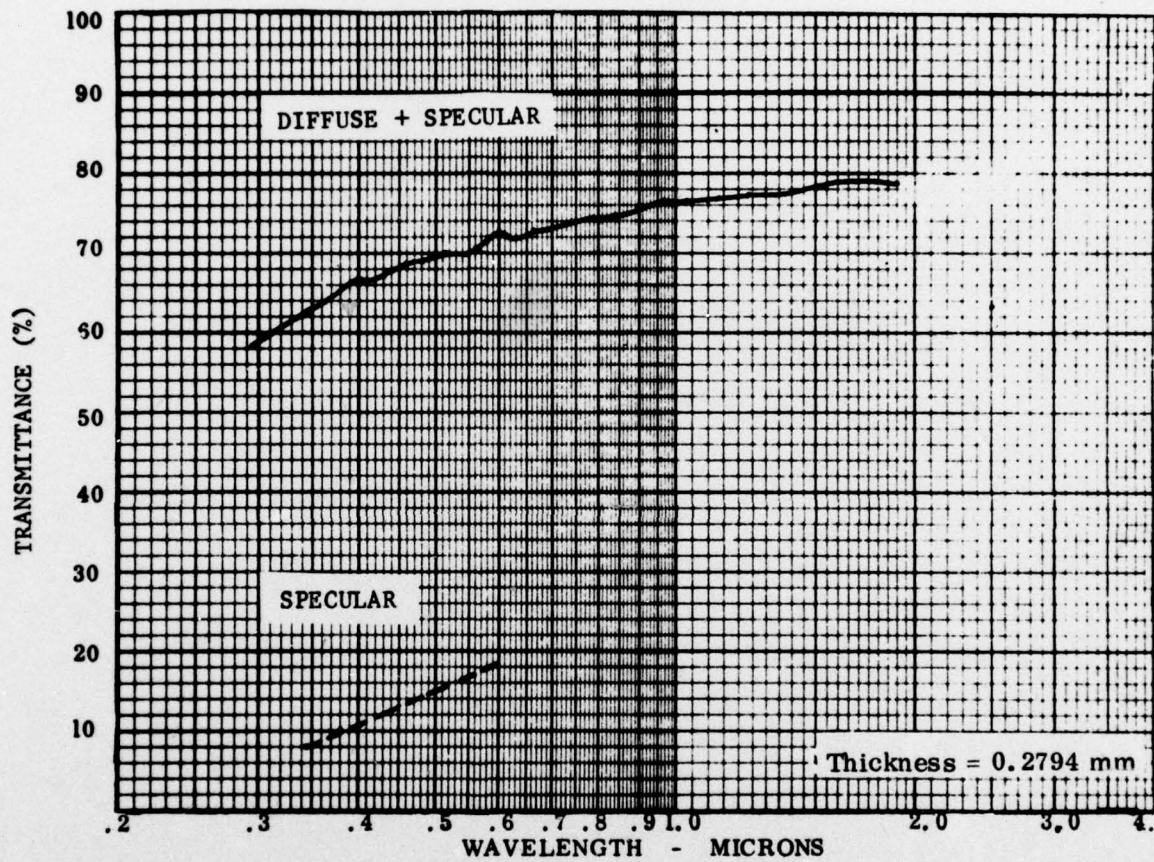
Figure 19. Hemispherical and Specular Visible Transmittance of Polished Flat Plate α -Si$_3$N$_4$ from Run No. 10. Specimen Thickness = 0.2794 mm.
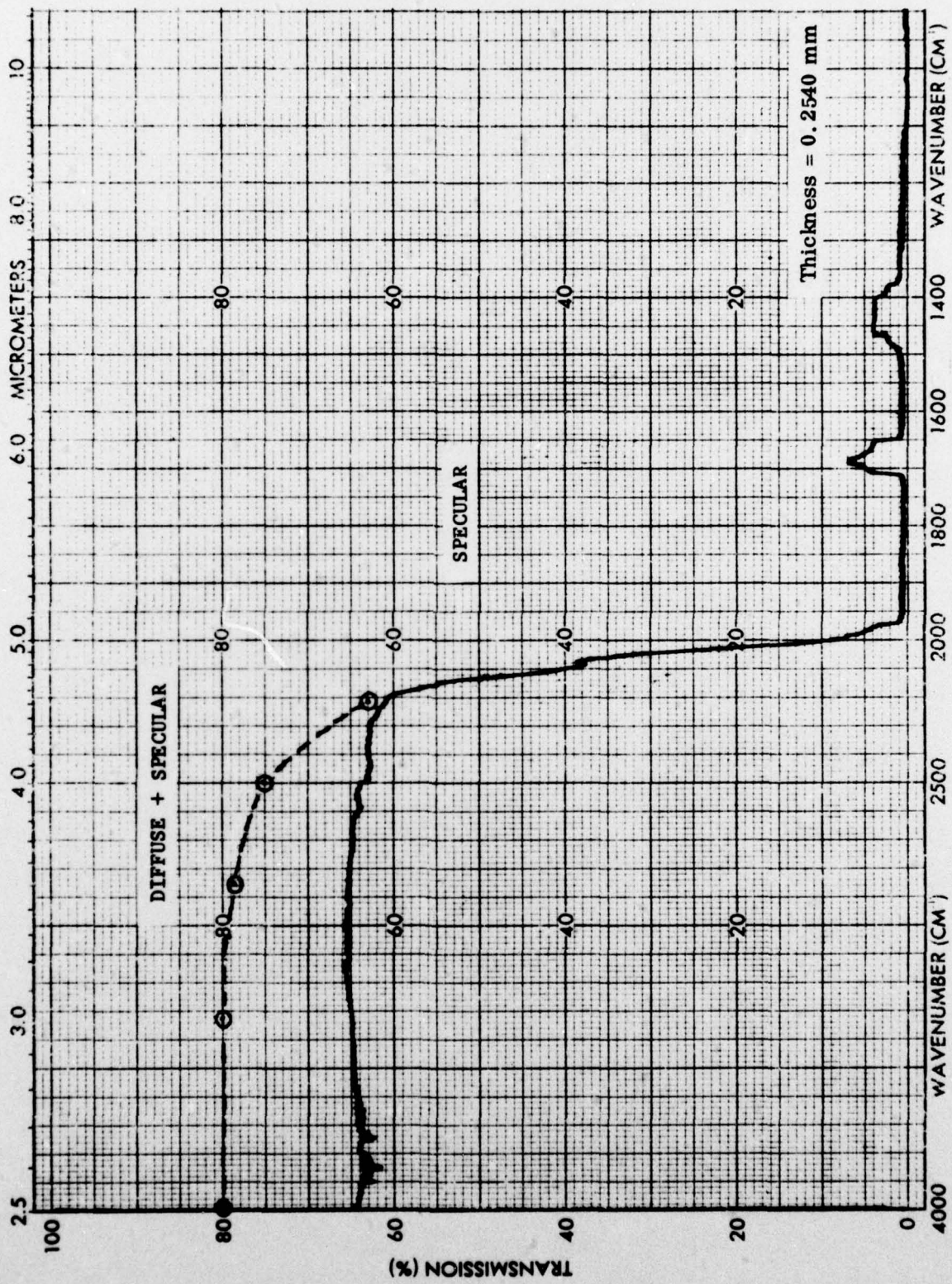
Figure 20. Hemispherical and Specular Infrared Transmittance of Polished Flat Plate α -Si_3N_4 from Run No. 9. Specimen Thickness = 0.2540 mm.
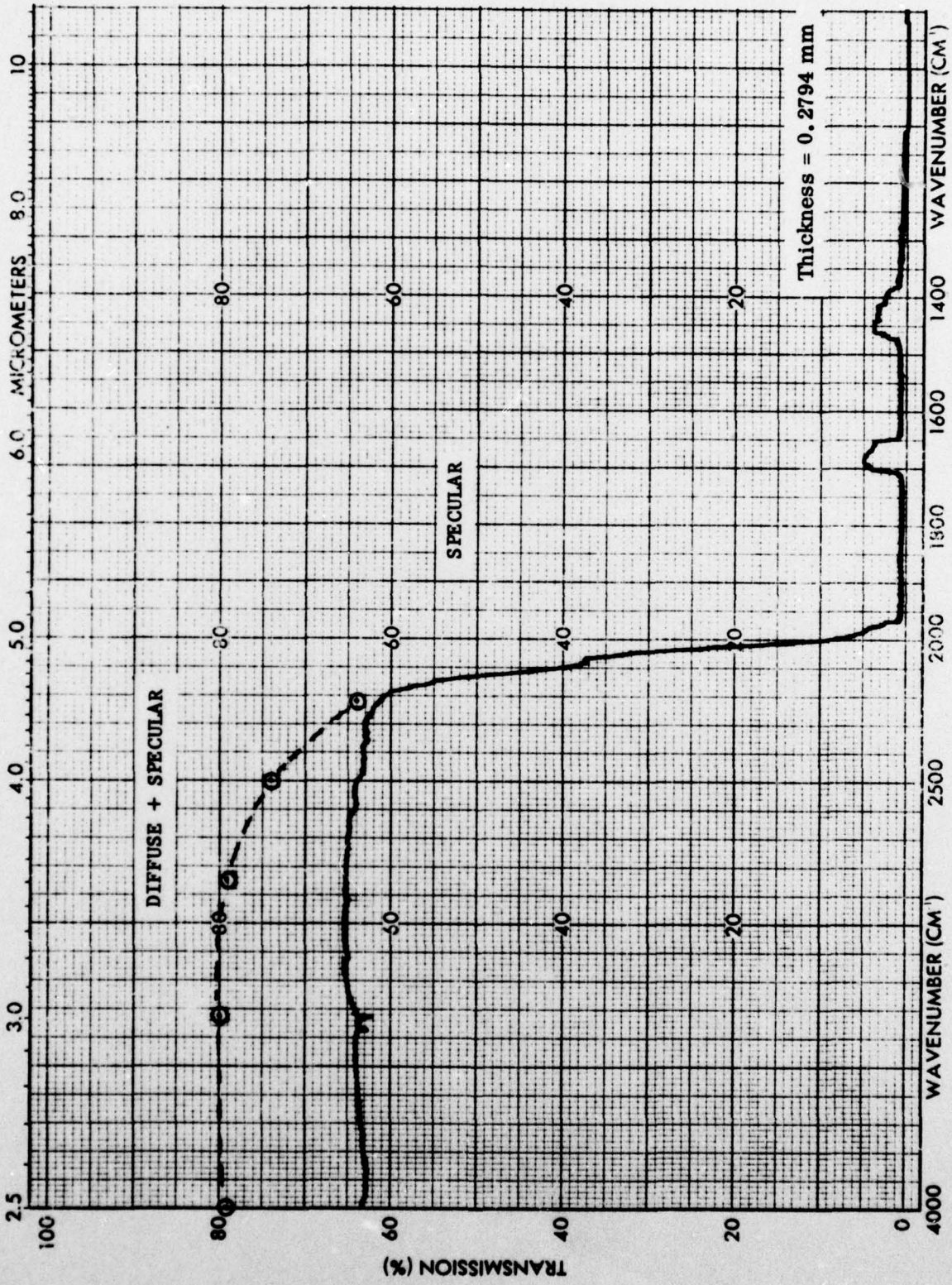
Figure 21. Hemispherical & Specular Infrared Transmittance of Polished Flat Plate α -Si$_3$N$_4$ from Run No. 10. Specimen Thickness = 0.2794 mm.
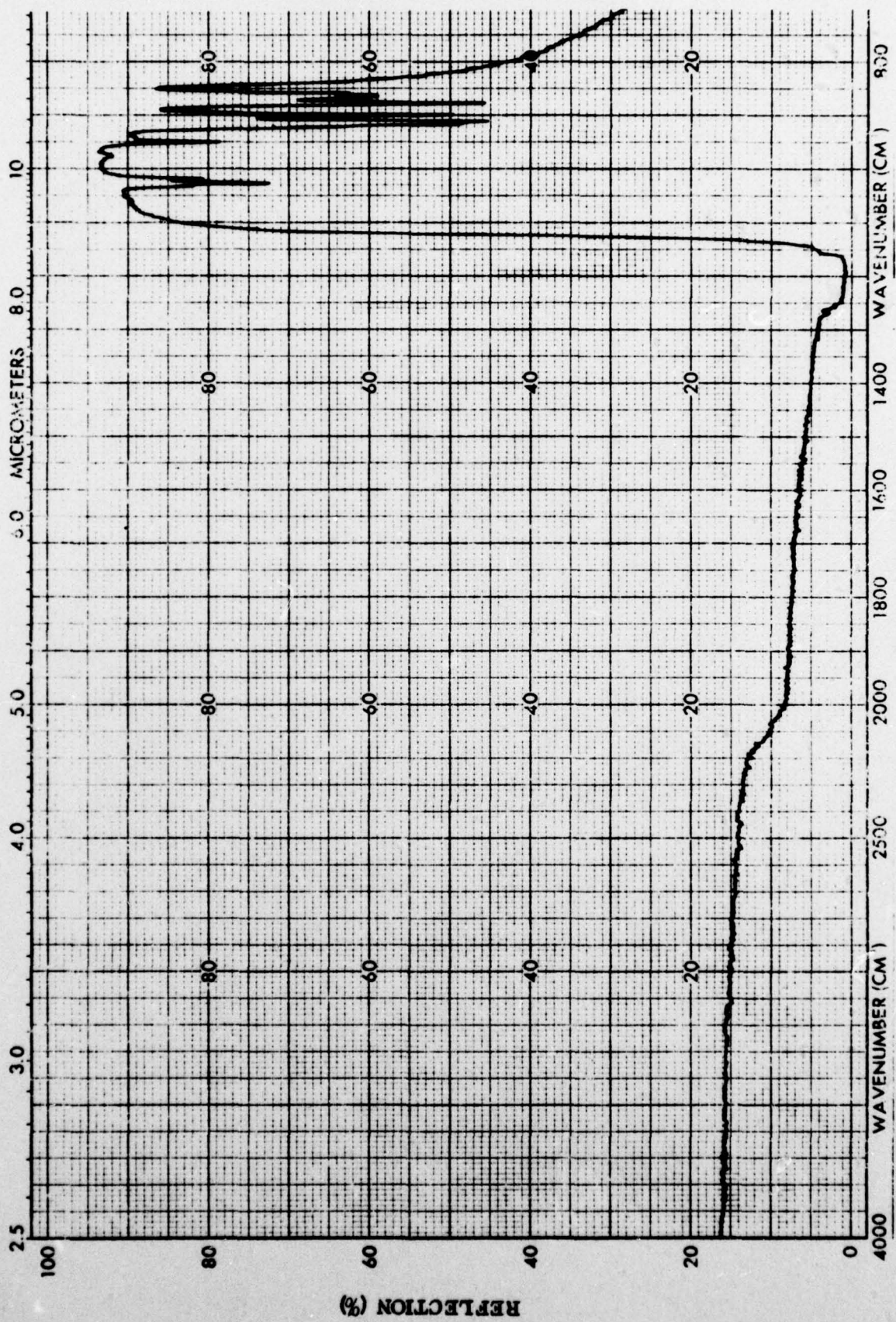
Figure 22. Specular Reflectance of Polished Flat Plate α-Si$_3$N$_4$ from Run No. 9. Specimen Thickness = 0.2540 mm.
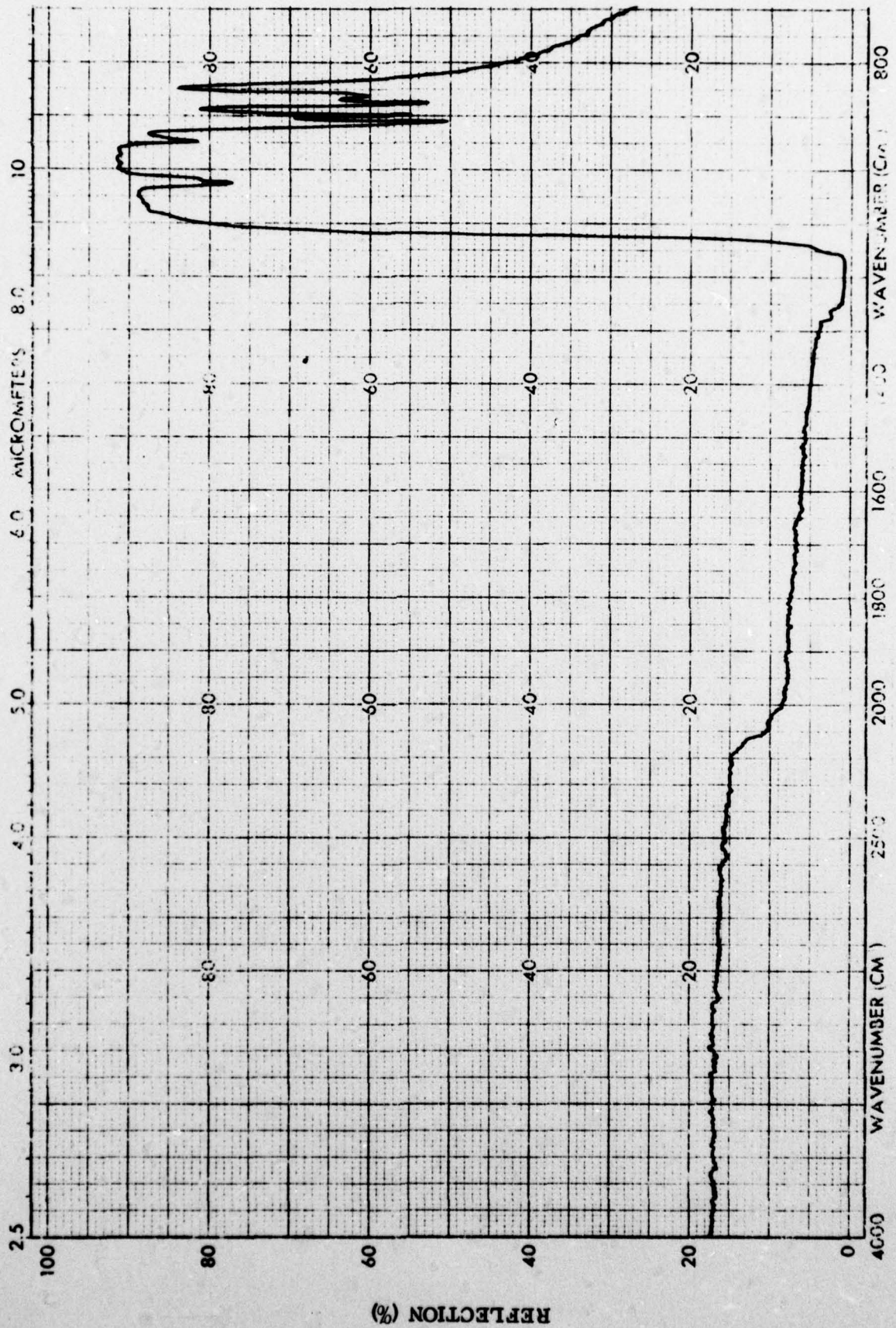
Figure 23. Specular Reflectance of Polished Flat Plate α-Si_3N_4 from Run No. 10. Specimen Thickness = 0.2794 mm
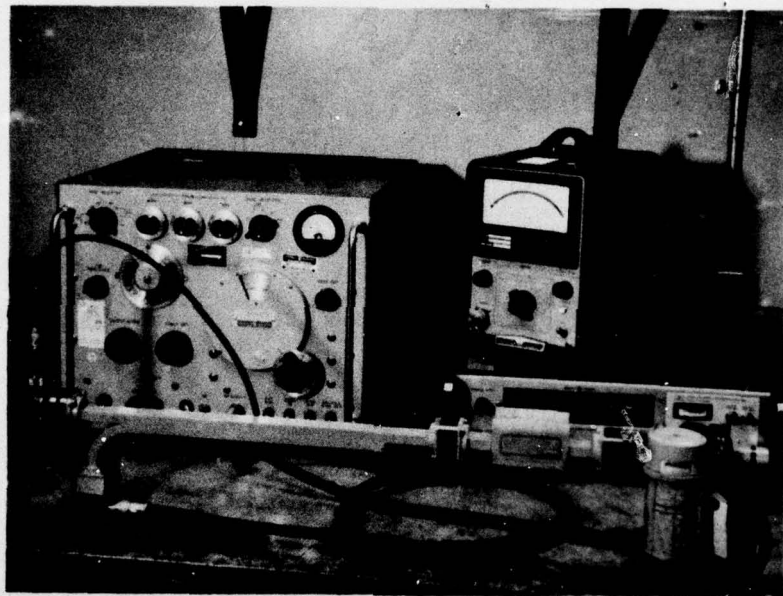
Figure 24. Laboratory Set-up for Determining Dielectric Properties
Using the Resonant Cavity Technique.

Table 6: Dielectric Properties of CVD α- Si_3N_4 at X-Band Frequency ($\sim$ 10 GHz)

Specimen	Dielectric Constant	Loss Tangent
Run No. 9, Spec. 1	7.90	0.0002
Run No. 10, Spec. 1	7.69	0.0006
Run No. 10, Spec. 2	7.62	0.0006

the future of CVD α-Si$_3$N$_4$ as a high temperature radar transmitting window is promising.

4.2.6 Thermal Expansion

The thermal expansion behavior of CVD α-Si$_3$N$_4$ (Run No. 10) was determined over the temperature range from room temperature to 1200°C. Figure 25 shows the thermal expansion vs. temperature function. A summary of thermal expansion coefficient data computed from the data in Figure 25 is given in Table 7.
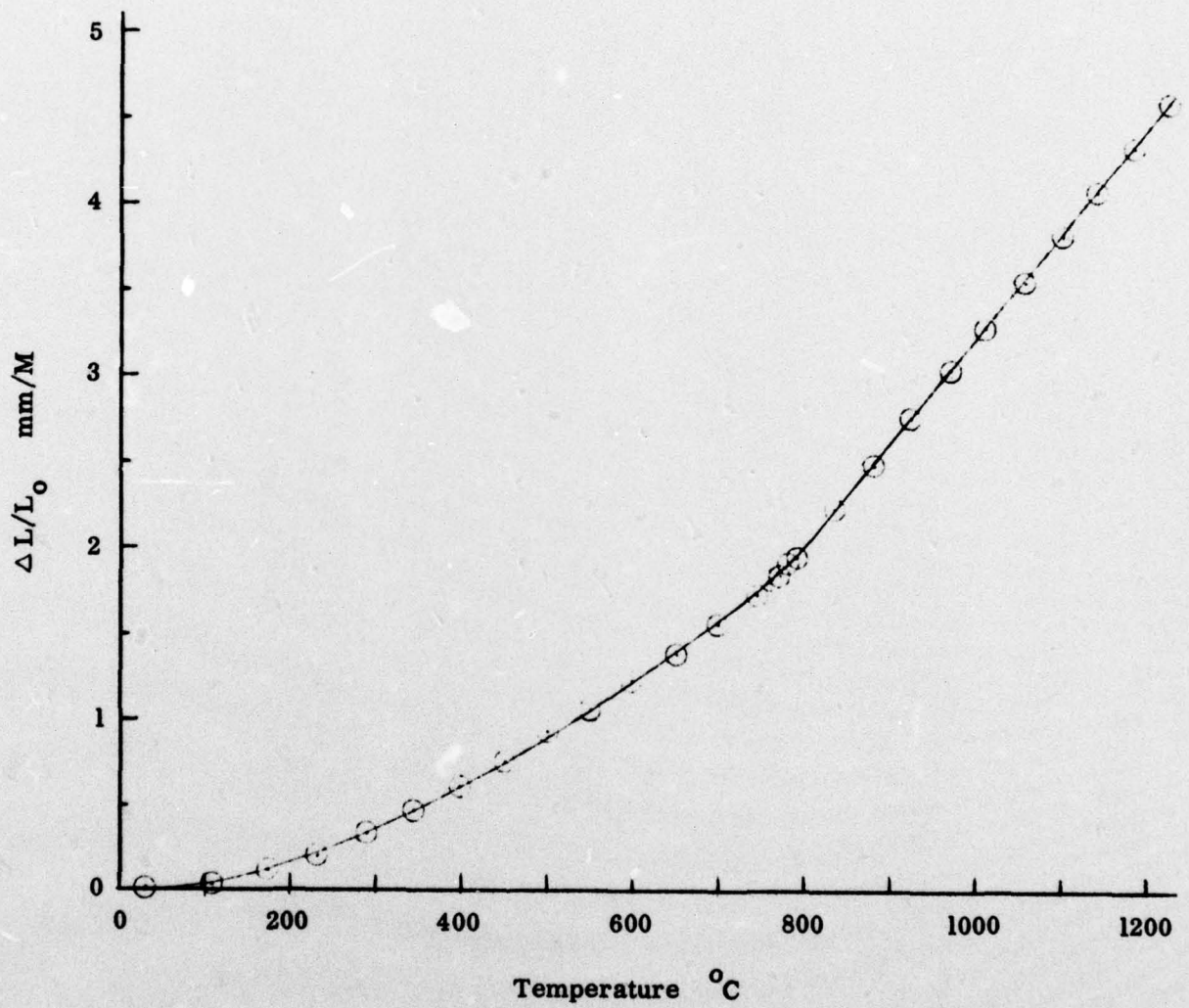
Figure 25. Thermal Expansion of CVD α -Si₃N₄ as a Function of Temperature Run No. 10.

Table 7: Thermal Expansion Coefficients of CVD α-Si_3N_4 (Run No. 10)

Temperature (^oC)	Thermal Expansion Coeff. ($1/^oC$)
290	0.336×10^{-6}
500	0.924×10^{-6}
781	1.907×10^{-6}
1013	3.284×10^{-6}
1224	4.594×10^{-6}

SECTION 5.0

CONCLUSIONS

Experimental work on this contract during the past year has led to the following conclusions:

1. Process parameters and mandrel configurations were identified for depositing flat plate and dome geometries with as-deposited thicknesses in the 1 to 2 mm range.

2. The highest deposition rate (up to 0.64 mm/hr) and conversion was obtained using $SiCl_4$ as the source of elemental silicon.

3. The SiF_4 reactant, while providing a relatively smooth last deposited surface, provided low deposition rates (up to 0.10 mm/hr) and conversion.

4. Dilute mixtures of the SiH_4 reactant resulted in the lowest deposition rates with as-deposited thicknesses to small to enable physical property characterizations other than surface morphology.

5. On the basis of future scale-up considerations, the use of $SiCl_4$ as the source of silicon (together with NH_3 and an H_2 carrier gas) appears to be the best reactant system in terms of raw material cost, conversion and deposition rate (provided that control of last deposited surface morphology is forthcoming).

6. The visible and infrared transmittance window for α-Si_3N_4 extends from below 0.20 microns to approximately 5.0 microns.

7. The visible colors of polished α-Si_3N_4 deposits include: beige, green, light to dark brown, and colorless (water-clear).

8. The apparent high-purity of CVD prepared α-Si_3N_4 produced on the program has resulted in microwave loss tangent data at X-band frequencies significantly below state-of-the-art Si_3N_4 material; if this trend continues at elevated temperatures, the application of CVD α-Si_3N_4 as a high temperature radar transmitting window is promising.

49.

9. Although room temperature flexure strength of CVD α-Si_3N_4 (at its current development stage in our laboratory) is approximately one-third that of state-of-the-art hot-pressed material, improvements in this level through control of grain morphology appear feasible. Supporting mechanical property data from NRL indicate unmatched strength retention (compared to other forms of Si_3N_4).

10. Crystalline CVD α-Si_3N_4 has hardness levels superior to common abrasives ranking it in third place behind diamond and cubic boron nitride; the hardness of amorphous CVD α-Si_3N_4, although somewhat lower than crystalline material, is comparable to α-Al_2O_3.

11. Supporting fracture toughness data from NRL and RI on CVD material prepared on this program indicate K_c levels approaching those of hot-pressed Si_3N_4, data suggests that achievement of finer grain size will increase K_c levels. (See Section 7.0, Appendix.)

SECTION 6.0

RECOMMENDATIONS

An assessment of the current status of CVD Si_3N_4 process developments in this laboratory as a result of the first year's contract activity has resulted in the following recommendations for future work:

1. Future processing research should now focus upon the development and control of a fine-grained microstructure to improve strength properties of crystalline deposits.

2. On the basis of future manufacturing considerations, the use of $SiCl_4$ as the source of silicon, NH_3 as the source of nitrogen and H_2 as the carrier gas should be emphasized in future process studies as a result of its lower raw material cost, higher conversion and higher deposition rate.

3. Increases and control of deposition rate must be addressed in future work to provide flat plate material of adequate thickness to enable comprehensive physical property characteristics.

4. The origin and control of visible color in CVD Si_3N_4 should be investigated; these variations and their origin are of obvious concern for ultraviolet and visible window applications, and may also have less obvious effects on other physical properties.

5. An assessment should be made with regard to the imaging potential of CVD α -Si_3N_4 in the visible and infrared wavelength regime; in this regard, the potential of amorphous CVD Si_3N_4 should be determined since optical isotropy would be anticipated for this morphology.

6. Continued characterization of key physical properties of interest for various DoD applications should be pursued with emphasis on high temperature behavior.

APPENDIX: FRACTURE TOUGHNESS AND IMPACT BEHAVIOR
OF CVD α-Si$_3$N$_4$

7.1 Introduction

An early estimate of the fracture toughness of CVD-prepared α-Si$_3$N$_4$ (extracted from Run Nos. 9 and 10) was obtained through the courtesy of Dr. S. W. Freiman of the Naval Research Lab (NRL) and Dr. A. G. Evans of Rockwell International (RI). The experimental work was supported by concurrent ONR programs at each laboratory, respectively.

7.2 NRL Measurements

The critical stress intensity factor (K_c) in the NRL work was deduced from critical fracture energy (γc) measurements using the ground double-cantilever test method.[19] An average critical fracture energy (γc) of 29.7 J/m^2 was obtained on four specimens from Run No. 9. The critical stress intensity factor, K_c, was obtained from the following equation:

$$K_c = \sqrt{2 \gamma_c E}$$

where E is the modulus of elasticity

γ_c is the critical fracture energy.

A K_c of 4.31 MPa $\sqrt{m}$ was arrived at using an average E of 312.14 GN/m^2 which was deduced from four-point flexure measurements (Table 5) on material from Run No. 9.

7.3 RI Measurements

An alternate test method was used by Evans at RI for determining the fracture toughness of CVD-prepared α-Si$_3$N$_4$ on specimens extracted from Run Nos. 9 and 10. The method uses identation fracture information obtained from

Vickers microhardness indenter data in the load region where measurable crack extension occurs from the corners of the diamond pyramid impression.[20] Figure 26 shows a typical experimental indenter impression for CVD material evaluated in this study (Run No. 9). From this data, the ratio of the crack extension from the centroid of the indenter impression, C, to the approximate indenter radius, a, is computed. (See Figure 26.) The fracture toughness is then computed from the normalized ordinate parameter, $\dfrac{K_c \; \emptyset}{H \; \sqrt{a}} \left(\dfrac{H}{\emptyset \, E} \right)^{0.4}$,

where H is the macrohardness associated with a given impression radius, a; E is the modulus of elasticity and $\emptyset$ is a constraint factor equal to 3.0. (See Figure 27.) Using this correlation, an average critical stress intensity factor, K_c, for material from Run Nos. 9 and 10, was found to be 3.2 MPa $\sqrt{m}$ (about 35 percent lower than the NRL measurements).

7.4 Discussion of Results

A 35 percent discrepancy in K_c is not too surprising considering the basic differences in the test methods. In the case of the NRL data, K_c values comparable to hot pressed Si_3N_4 (as measured at NRL) were obtained. On the other hand, the RI data falls somewhere between reaction sintered Si_3N_4 (K_c = 2.2 MPa $\sqrt{m}$) and hot-pressed Si_3N_4 (K_c = 5.0 MPa $\sqrt{m}$) data as measured by the RI indenter technique. The higher values of the NRL data (compared to the RI data on CVD α -Si_3N_4 is possibly due to the fact that the NRL method involves crack growth phenomena extending across several grains, whereby the RI crack extension occurs over only a few grains at most, thus providing data more representative of single crystal material. Also, the RI data represents near surface properties rather than a bulk property as determined by the NRL method. For finer grain size microstructures, the two test methods should yield better agreement with K_c values comparable, or possibly exceeding, hot-pressed Si_3N_4.

Figure 26. Identation Fracture of CVD α -Si$_3$N$_4$ (Run No. 9).
Identer Load   10 kg.
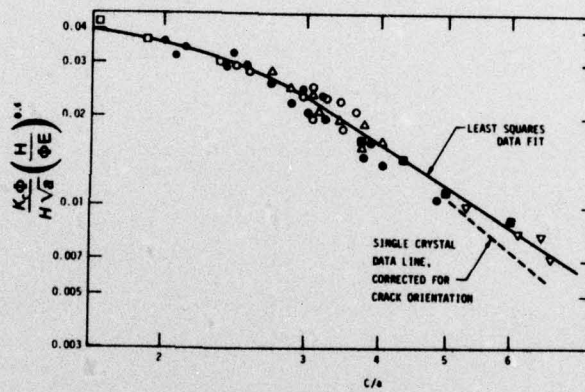
Figure 27. Correlation of the Critical Stress Intensity
Factor (K_C) with Radial Crack Extension Data[20]

55.

SECTION 8.0

REFERENCES

1. C. Greskovich, J.H. Rosolowski and S. Prochazka, ARPA Final Technical Report, No. SR -75-084, 1975 (ONR Contract No. N00014-74-C-0331).

2. K. Niihara and T. Hirai, J. Mat. Sci., 12 (1977), 1243-1252.

3. MCIC-HB-07, "Engineering Property Data on Selected Ceramics, Vol. 1, Nitrides", March 1976, p. 5.3.3.-28.

4. K.E. Bean, P.S. Geim, R.L. Yeakley and W.R. Runyan, J. Electrochem. Soc., 114, (1967), 733.

5. V.Y. Doo, D.R Kerr and D.R. Nichols, ibid, 115, (1978), 61.

6. M. Billy, Ann. Chem., (13), 4, (1959), 795-851; Compt. rend. 250 (1960), 4163-64.

7. K.S. Mazdiyasni and C.M. Cooke, J. Am. Ceram. Soc., 56, (1973), 628.

8. M. Billy, Bull. Soc. Chim. (France), 1960, 1653-54.

9. A. Warden, Chem. Ind. (London), 1970, (10), 338-339.

10. A.C Airey, S. Clarke and P. Popper, Trans. Brit. Ceram. Soc., 22, (1973), 305-320.

11. G. Cohet, H. Mellottee and R. Delbourgo, Proc. 5th. Int. Conf. on CVD, Electrochem. Soc., Princeton, NJ, 1975, p. 43-56.

12. J.J. Gebhardt, R.A. Tanzilli, and T.A. Harris, J. Electrochem. Soc., 123, (10), (1976), 1578-83.

13. K. Niihara and T. Hirai, J. Mat. Sci., 12, (1977), 1233-1242.

14. K. Niihara and T. Hirai, J. Mat. Sci., 11, (1976), 593-603, 604-611.

15. F. Galasso, V. Kuntz and W.J. Croft, J. Am. Ceram. Soc., 55, (1972), 431.

16. United Aircraft. Brit. Pat. 1,063,305, Marc. 30, 1967.

17. K. Kijima, N. Setaka and H. Tanaka, J. Cryst. Growth, 24/25, (1974), 183-187.

18. O.O. Adewoye et. al., "Structural Studies of Surface Deformation in MgO, SiC and Si_3N_4", AD-A008 993, Oct. 1974, p. 28.

19. S. W. Freiman, D. R. Mulville, and P. W. Mast, J. Mater. Sci., $\underline{8}$, [11], 1527, (1973).

20. A. G. Evans and E. A. Charles, J. Am. Cer. Soc., $\underline{59}$, [7-8], 371, (1976).

Technical and Summary Reports

Organization	No. of Copies	Organization	No. of Copies
Defense Documentation Center Cameron Station Alexandria, Virginia 22314	(12)	Naval Construction Batallion Civil Engineering Laboratory Port Hueneme, California 93043 Attn: Materials Division	(1)

Office of Naval Research
Department of the Navy
Arlington, Virginia 22217
Attn: Code 471
     Code 102
     Code 470
	(3)
	(1)
	(1)
		Naval Electronics Laboratory Center
		San Diego, California 92152
		Attn: Electron Materials
		     Sciences Division
			(1)

Commanding Officer Office of Naval Research Branch Office 495 Summer Street Boston, Massachusetts 02210	(1)	Naval Missile Center Materials Consultant Code 3312-1 Point Mugu, California 93041	(1)
Commanding Officer Office of Naval Research Branch Office 536 South Clark Street Chicago, Illinois 60605	(1)	Commanding Officer Naval Surface Weapons Center White Oak Laboratory Silver Spring, Maryland 20910 Attn: Library	(1)
Office of Naval Research San Francisco Area Office 760 Market Street, Room 447 San Francisco, California 94102 Attn: Dr. P.A. Miller	(1)	David W. Taylor Naval Ship R&D Center Materials Department Annapolis, Maryland 21402	(1)
Naval Research Laboratory Washington, D.C. 20390		Naval Undersea Center San Diego, California 92132 Attn: Library	(1)

Attn: Code 6000
     Code 6100
     Code 6300
     Code 6400
     Code 2627
	(1)
	(1)
	(1)
	(1)
	(1)
		Naval Underwater System Center
		Newport, Rhode Island 02840
		Attn: Library
		
		Naval Weapons Center
		China Lake, California 93555
		Attn: Library
			(1)
			
			(1)

Naval Air Development Center Code 302 Warminster, Pennsylvania 18974 Attn: Mr. F.S. Williams	(1)	Naval Postgraduate School Monterey, California 93940 Attn: Mechanical Engineering Dept.	(1)

Naval Air Propulsion Test Center
Trenton, New Jersey 08628
Attn: Library
	(1)	Naval Air Systems Command
		Washington, D.C. 20360
		
		Attn: Code 52031
		     Code 52032
		     Code 320
			
			(1)
			(1)
			(1)

Organization	No. of Copies	Organization	No. of Copies
Naval Sea System Command Washington, D.C. 20362 Attn: M. Kinna, Code 035	(1)	NASA Headquarters Washington, D.C. 20546 Attn: Code RRM	(1)
Naval Facilities Engineering Command Alexandria, Virginia 22331 Attn: Code 03	(1)	NASA Lewis Research Center 21000 Brookpark Road Cleveland, Ohio 44135 Attn: Library	
Scientific Advisor Commandant of the Marine Corps Washington, D.C. 20380 Attn: Code AX	(1)	National Bureau of Standards Washington, D.C. 20234	
		Attn: Metallurgy Division Inorganic Materials Division	(1) (1)
Naval Ship Engineering Center Department of the Navy CTR BG #2 3700 East-West Highway Prince Georges Plaza Hyattsville, Maryland 20782 Attn: Engineering Materials and Services Office, Code 6101	(1)	Defense Metals and Ceramics Information Center Battelle Memorial Institute 505 King Avenue Columbus, Ohio 43201	(1)
Army Research Office Box CM, Duke Station Durham, North Carolina 27706 Attn: Metallurgy & Ceramics Div.	(1)	Director Ordnance Research Laboratory P.O. Box 30 State College, Pennsylvania 16801	(1)
Army Materials and Mechanics Research Center Watertown, Massachusetts 02172 Attn: Res. Programs Office (AMXMR-P)	(1)	Director Applied Physics Laboratory University of Washington 1013 Northeast Fortieth Street Seattle, Washington 98105	(1)
Air Force Office of Scientific Research Bldg. 410 Bolling Air Force Base Washington, D.C. 20332 Attn: Chemical Science Directorate Electronics and Solid State Sciences Directorate	(1) (1)	Metals and Ceramics Division Oak Ridge National Laboratory P.O. Box X Oak Ridge, Tennessee 37380	(1)
		Los Alamos Scientific Laboratory P.O. Box 1663 Los Alamos, New Mexico 87544 Attn: Report Librarian	(1)
Air Force Materials Lab (LA) Wright-Patterson AFB Dayton, Ohio 45433	(1)	Argonne National Laboratory Metallurgy Division P.O. Box 229 Lemont, Illinois 60439	(1)

Organization	No. of Copies	Organization	No. of Copies
Brookhaven National Laboratory Technical Information Division Upton, Long Island New York 11973 Attn: Research Library	(1)		
Library Building 50 Room 134 Lawrence Radiation Laboratory Berkeley, California	(1)		

Technical and Summary Reports

Organization	No. of Copies	Organization	No. of Copies
Dr. W.F. Adler Effects Technology Inc. 5383 Hollister Avenue P.O. Box 30400 Santa Barbara, CA 92105	(1)	Professor A.H. Heuer Case Western Reserve University University Circle Cleveland, OH 44106	(1)
Dr. G. Bansal Battelle 505 King Avenue Columbus, OH 43201	(1)	Dr. R. Hoagland Battelle 505 King Avenue Columbus, OH 43201	(1)
Dr. R. Bratton Westinghouse Research Lab. Pittsburgh, PA 15235	(1)	Dr. R. Jaffee Electric Power Research Institute Palo Alto, CA	(1)
Dr. A.G. Evans Rockwell International P.O. Box 1085 1049 Camino Dos Rios Thousand Oaks, CA 91360	(1)	Dr. P. Jorgensen Stanford Research Institute Poulter Laboratory Menlo Park, CA 94025	(1)
Mr. E. Fisher Ford Motor Co. Dearborn, MI	(1)	Dr. R.N. Katz Army Materials and Mechanics Research Center Watertown, MA 02171	(1)
Dr. P. Gielisse University of Rhode Island Kingston, RI 02881	(1)	Dr. H. Kirchner Ceramic Finishing Company P.O. Box 498 State College, PA 16801	(1)
Dr. M.E. Gulden International Harvester Company Solar Division 2200 Pacific Highway San Diego, CA 92138	(1)	Dr. B. Koepke Honeywell, Inc. Corporate Research Center 500 Washington Avenue, South Hopkins, MN 55343	(1)
Dr. D.P.H. Hasselman Montana Energy and MHD Research and Development Institute P.O. Box 3809 Butte, Montana 59701	(1)	Mr. Frank Koubek Naval Surface Weapons Center White Oak Laboratory Silver Spring, MD 20910	(1)
Mr. G. Hayes Naval Weapons Center China Lake, CA 93555	(1)	E. Krafft Carborundum Co. Niagara Falls, NY	(1)

Organization	No. of Copies	Organization	No. of Copies
Dr. F.F. Lange Rockwell International P.O. Box 1085 1049 Camino Dos Rios Thousand Oaks, CA 91360	(1)	Dr. J. Ritter University of Massachusetts Department of Mechanical Engineering Amherst, MA 01002	(1)
Dr. J. Lankford Southwest Research Institute 8500 Culebra Road San Antonio, TX 78284	(1)	Professor R. Roy Pennsylvania State University Materials Research Laboratory University Park, PA 16802	(1)
Library Norton Company Industrial Ceramics Division Worcester, MA 01606	(1)	Dr. R. Ruh AFML Wright-Patterson AFB Dayton, OH 45433	(1)
State University of New York College of Ceramics at Alfred University Attn: Library Alfred, NY 14802	(1)	Mr. J. Schuldies AiResearch Phoenix, AZ	(1)
Dr. L. Hench University of Florida Ceramics Division Gainesville, FL 32601	(1)	Professor G. Sines University of California, Los Angeles Los Angeles, CA 90024	(1)
Dr. N. MacMillan Materials Research Laboratory Pennsylvania State University College Park, PA 16802	(1)	Dr. N. Tallan AFML Wright-Patterson AFB Dayton, OH 45433	(1)
Mr. F. Markarian Naval Weapons Center China Lake, CA 93555	(1)	Dr. T. Vasilos AVCO Corporation Research and Advanced Development Division 201 Lowell Street Wilmington, MA 01887	(1)
Dr. Perry A. Miles Raytheon Company Research Division 28 Seyon Street Waltham, MA 02154	(1)	Mr. J.D. Walton Engineering Experiment Station Georgia Institute of Technology Atlanta, GA 30332	(1)
Mr. R. Rice Naval Research Laboratory Code 6360 Washington, D.C. 20375	(1)	Dr. S.M. Widerhorn Inorganic Materials Division National Bureau of Standards Washington, DC 20234	(1)

Organization	No. of Copies	Organization	No. of Copies
Dr. S.A. Bortz IITRI 10 W. 35th Street Chicago, IL 60616	(1)	Major W. Simmons Air Force Office of Scientific Research Building 410 Bolling Air Force Base Washington, DC 20332	(1)
Mr. G. Schmitt Air Force Materials Laboratory Wright-Patterson AFB Dayton, OH 45433	(1)	Dr. P. Becher Naval Research Laboratory Code 6362 Washington, DC 20375	(1)
Dr. D.A. Shockey Stanford Research Institute Poulter Laboratory Menlo Park, CA 94025	(1)	Mr. L.B. Weckesser Applied Physics Laboratory Johns Hopkins Road Laurel, MD 20810	(1)
Dr. W.G.D. Frederick Air Force Materials Laboratory Wright-Patterson AFB Dayton, OH 45433	(1)	Mr. D. Richarson AiResearch Manufacturing Company 4023 36th Street P.O. Box 5217 Phoenix, AZ 85010	(1)
Dr. P. Land Air Force Materials Laboratory Wright-Patterson AFB Dayton, OH 45433	(1)	Dr. H.E. Bennett Naval Weapons Center Code 3818 China Lake, CA 93555	(1)
Mr. K. Letson Redstone Arsenal Huntsville, AL 35809	(1)	Mr. G. Denman Air Force Materials Laboratory Code LPJ Wright-Patterson AFB Dayton, OH 45433	(1)
Dr. S. Freiman Naval Research Laboratory Code 6363 Washington, DC 20375	(1)		
Director Materials Sciences Defense Advanced Research Projects Agency 1400 Wilson Boulevard Arlington, VA 22209	(1)	Dr. D. Godfrey Admiralty Materials Laboratory Polle, Dorset BH16 6JU UNITED KINGDOM	(1)
Dr. James Pappis Raytheon Company Research Division 28 Seyon Street Waltham, MA 02154	(1)	Dr. N. Corney Ministry of Defense The Adelphi John Adam Street London WC2N 6BB UNITED KINGDOM	(1)

Organization	No. of Copies	Organization	No. of Copies
Dr. L.M. Gillin Aeronautical Research Laboratory P.O. Box 4331 Fisherman's Bend Melbourne, VIC 3001 AUSTRALIA	(1)		
T. Paquette 5390 Cherokee Avenue Alexandria, VA 22314	(1)		